Chapter 11

Jets and Missing Transverse Energy

The huge QCD cross section (Fig. 11.1) ensures that jets will dominate high-p_{T} physics at the LHC. Jets will not only provide a benchmark for understanding the detector, but will also serve as an important tool in the search for physics beyond the standard model. Event signatures for SUSY, Higgs boson production, compositeness, and other new physics processes require accurate reconstruction and measurement of jets coming from high-p_{T} quarks and gluons [246]–[249]. The problems with associating a jet measured in a calorimeter with a scattered parton is an old, persistent problem in hadron collisions [250]–[256]. Jet energy resolution and linearity are key factors in separating signal events from backgrounds. Missing transverse energy resolution, which historically has played an important role in the discoveries of the W boson and the top quark and the search for new phenomena at hadron colliders, is closely related to the calorimeter jet energy response.

A detailed description of the calorimeter response, including pulse shape, digitization and zero suppression have been simulated with high statistics. Monte Carlo simulation samples of fully simulated events at the detector level have been used to study jet and missing transverse energy response. The calibration procedures described in Chapter 5, together with these simulations, give an idea of the jet and missing transverse energy performance at startup. The commissioning phase of the detector will have a tremendous impact on understanding the calorimeter reponse and will help to refine plans for data-driven calibrations and jet energy scale determination.

11.1 Tower definition and thresholds

Readout cells in HCAL are arranged in a tower pattern in η, ϕ space, projective to the nominal interaction point. The cells in the barrel region have segmentation of $\Delta\eta \times \Delta\phi = 0.087 \times 0.087$, becoming progressively larger in the endcap and forward regions. Since the ECAL granularity is much finer than HCAL, calorimeter towers (ECAL plus HCAL) are formed by addition of signals in η, ϕ bins corresponding to individual HCAL cells. In total there are 4176 such towers, which when unfolded, may be represented in a familiar "lego" plot (Fig. 11.2).

The towers are used as input to several jet clustering algorithms. The energy associated with a tower is calculated as the sum of all contributing readout cells which pass the online zero-suppression threshold and any additional offline software thresholds. For the purpose of jet clustering, the towers are treated as massless particles, with the energy given by the tower energy, and the direction defined by the interaction point and the center of the tower.

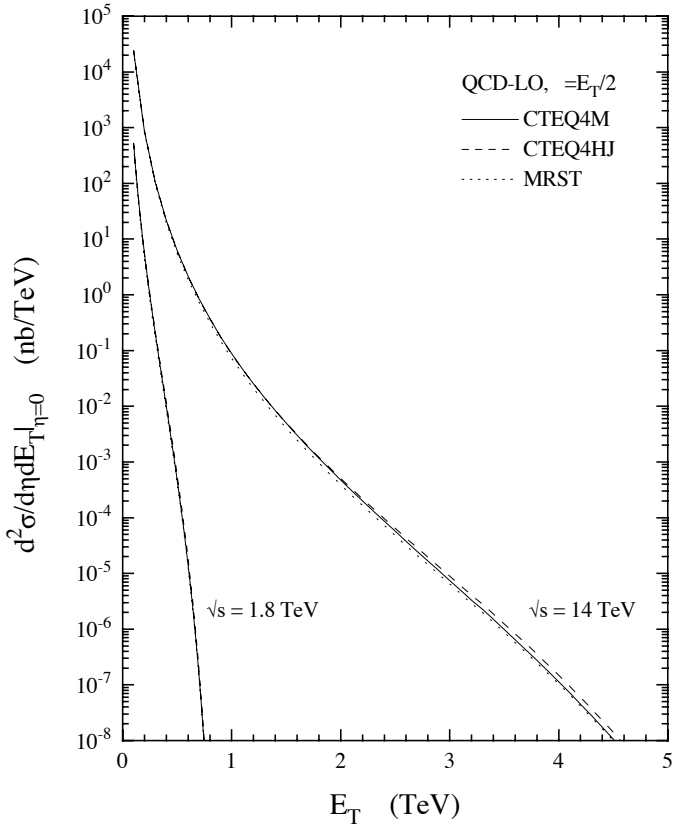

Figure 11.1: Inclusive jet cross section vs. jet transverse energy at the LHC compared with the Tevatron [257]. The cross section is 7 orders of magnitude greater at the LHC than at the Tevatron kinematic limit, and the luminosity will also be more than 2 orders of magnitude greater.

Optimum performance of higher-level objects reconstructed from calorimeter towers requires careful selection of these inputs because calorimeter noise contributions can have significant impact on the reconstruction of low-E_{T} jets. Various schemes of suppressing contributions of noise and pile-up to jet energies have been studied in detail [258], based on simulation of calorimeter response as implemented in ORCA. These studies include variation of thresholds on the towers as well as the individual cells which constitute towers.

Usually either a transverse energy cut $E_{\mathrm{T}} > 0.5$ GeV or $E_{\mathrm{T}} > 0.5$ GeV and energy cut $E > 0.8$ GeV (scheme T) were applied to all towers used in jet reconstruction. While both approaches give similar results for high-E_{T} jets, the latter scheme eliminates more noise in the central η region, and is hence preferred for jet reconstruction at low E_{T}.

To further refine the noise rejection, energy thresholds applied to individual cells were investigated. It is a natural choice as the noise contribution depends on the type of the calorimeter compartment. HCAL cells show discrete ADC readout patterns (Fig. 5.8), with 1 ADC count corresponding to approximately 250 MeV in HB and HO, and 400 MeV HE. This quantization must be taken into account when setting thresholds. Three schemes referred to as A, B, and C in Table 11.1 were designed to increment the thresholds on HCAL cells in steps of an ADC count. As an example, the scheme A retains 1.4 GeV of noise in the $R = 0.5$ cone at

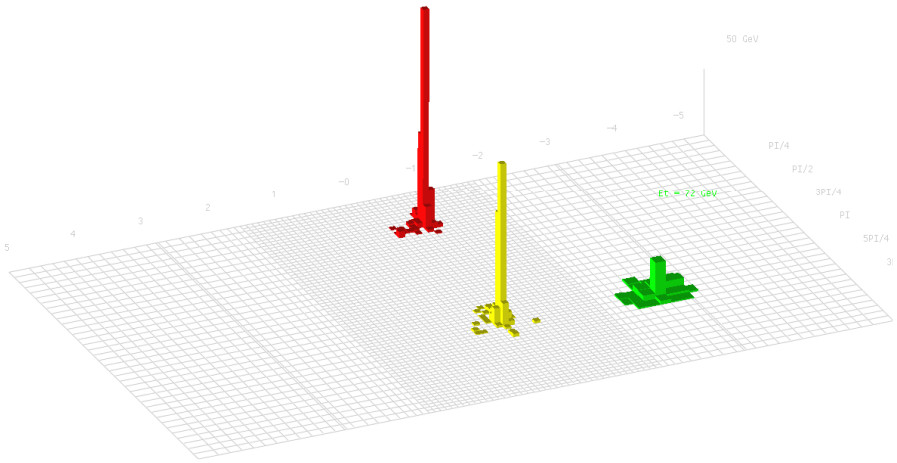

Figure 11.2: The η, ϕ segmentation of the CMS hadron calorimeter.

$\eta = 0$. In comparison, the tower-threshold scheme T has 0.6 GeV of noise, and 2.8 GeV more loss of jet energy on average in the QCD jet sample generated with $\hat{p}_{\mathrm{T}} > 40$ GeV/c (where $\hat{p}_{\mathrm{T}}$ is the parton p_{T} in the $2 \to 2$ scattering process in PYTHIA).

Table 11.1: Cell energy threshold schemes. Values are given in GeV. ΣEB (ΣEE) are thresholds on the total EB (EE) energy of all contributing ECAL crystals in a tower. NIC is the average noise-in-cone energy and JEL is the energy loss in a jet relative to scheme A for $R = 0.5$. NIC is measured in a noise sample and JEL is measured in a QCD40 sample without noise or pile-up included in the simulation. ΣE_{T} is the total transverse energy in the calorimeter.

Scheme	Thresholds					NIC	JEL	NIC	JEL	ΣE_{T}	ΣE_{T}
	HB	HO	HE	ΣEB	ΣEE	$\eta \simeq 0$	$\eta \simeq 0$	$\eta \simeq 2$	$\eta \simeq 2$	noise	QCD
A	0.7	0.85	0.9	0.2	0.45	1.4	–	1.1	–	28	168
B	0.9	1.1	1.4	0.2	0.45	0.3	1.0	0.4	2.7	6	162
C	1.2	1.3	1.8	0.2	0.45	0.2	1.9	0.3	5.2	4	158

The individual cell energy threshold schemes A and B decrease the noise to a manageable level while losing minimal amount of real energy. These 2 schemes should be used for noise suppression online or in future jet reconstruction and physics studies.

To compare jet reconstruction efficiencies for different threshold schemes, the minimum value of reconstructed jet E_{T} has been adjusted to give 50% efficiency at 20 GeV for each scheme separately; this procedure is intended to compensate for differences in the calibrations. These (uncorrected) jet thresholds are shown in Fig. 11.3 a as a function of generated jet E_{T} where the efficiency condition is imposed. The resulting efficiency curves (Fig. 11.3 b) are remarkably similar in shape indicating that the corresponding jet resolutions for the different threshold schemes are similar.

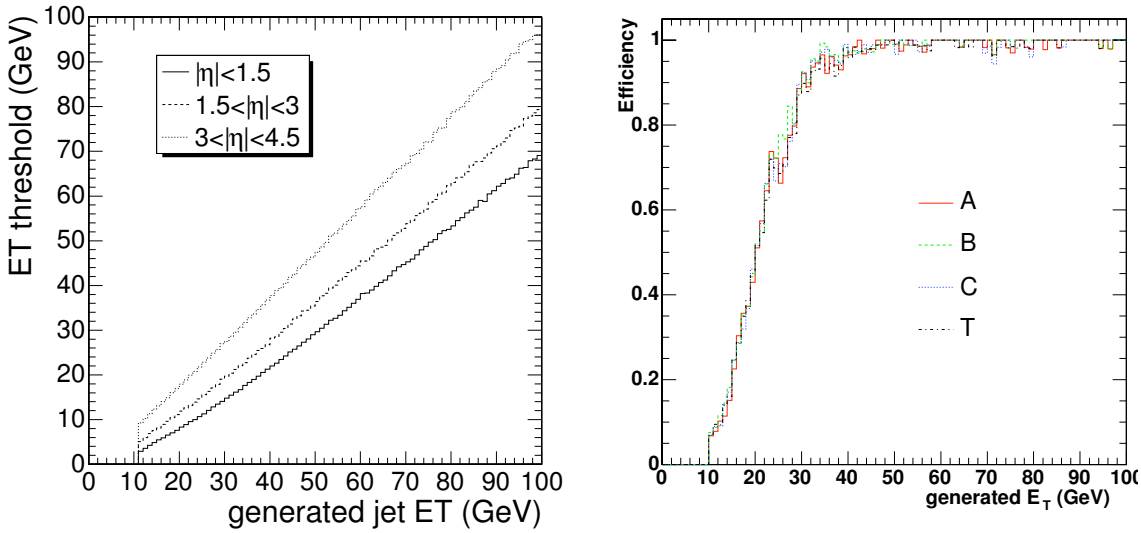

Figure 11.3: Left) Jet E_{T} threshold needed to reconstruct jets with 50% efficiency for the tower threshold scheme (T) with $E > 0.8$ GeV and $E_{\mathrm{T}} > 0.5$ GeV. Right) Jet efficiency curves for different threshold schemes and central η.

11.2 Jet algorithms

The first jet algorithms for hadron physics were simple cones [250, 259]. Over the last two decades, clustering techniques have greatly improved in sophistication. Three principal jet reconstruction algorithms have been coded and studied for CMS: the iterative cone [260], the midpoint cone [261] and the inclusive k_{T} jet algorithm [262, 263]. The midpoint-cone and k_{T} algorithms are widely used in offline analysis in current hadron collider experiments, while the iterative cone algorithm is simpler and faster and commonly used for jet reconstruction in software-based trigger systems.

The jet algorithms may be used with one of two recombination schemes for adding the constituents. In the energy scheme, constituents are simply added as four-vectors. This produces massive jets. In the E_{T} scheme, massless jets are produced by equating the jet transverse momentum to the ΣE_{T} of the constituents and then fixing the direction of the jet in one of two ways: 1) $\sin\theta = \Sigma E_{\mathrm{T}}/E$ where E is the jet energy (usually used with cone algorithms), or 2) $\eta = \Sigma E_{\mathrm{T}i}\eta_i/\Sigma E_{\mathrm{T}}$ and $\phi = \Sigma E_{\mathrm{T}i}\phi_i/\Sigma E_{\mathrm{T}}$ (usually used with the k_{T} algorithm). In all cases the jet E_{T} is equal to $p_{\mathrm{T}}c$.

The inclusive k_{T} algorithm merges, in each iteration step, input objects into possible final jets and so the new jet quantities, the jet direction and energy, have to be calculated directly during the clustering. The cone jet algorithms, iterative and midpoint, group the input objects together as an intermediate stage and the final determination of the jet quantities (recombination) is done in one step at the end of the jet finding.

11.2.1 Iterative cone

In the iterative cone algorithm, an E_{T}-ordered list of input objects (particles or calorimeter towers) is created. A cone of size R in η,ϕ space is cast around the input object having the

largest transverse energy above a specified seed threshold. The objects inside the cone are used to calculate a "proto-jet" direction and energy using the E_{T} scheme. The computed direction is used to seed a new proto-jet. The procedure is repeated until the energy of the proto-jet changes by less than 1% between iterations and the direction of the proto-jet changes by $\Delta R < 0.01$. When a stable proto-jet is found, all objects in the proto-jet are removed from the list of input objects and the stable proto-jet is added to the list of jets. The whole procedure is repeated until the list contains no more objects with an E_{T} above the seed threshold. The cone size and the seed threshold are parameters of the algorithm. When the algorithm is terminated, a different recombination scheme may be applied to jet constituents to define the final jet kinematic properties.

11.2.2 Midpoint cone

The midpont-cone algorithm was designed to facilitate the splitting and merging of jets. The midpoint-cone algorithm also uses an iterative procedure to find stable cones (proto-jets) starting from the cones around objects with an E_{T} above a seed threshold. In contrast to the iterative cone algorithm described above, no object is removed from the input list. This can result in overlapping proto-jets (a single input object may belong to several proto-jets). To ensure the collinear and infrared safety of the algorithm, a second iteration of the list of stable jets is done. For every pair of proto-jets that are closer than the cone diameter, a *midpoint* is calculated as the direction of the combined momentum. These midpoints are then used as additional seeds to find more proto-jets. When all proto-jets are found, the splitting and merging procedure is applied, starting with the highest E_{T} proto-jet. If the proto-jet does not share objects with other proto-jets, it is defined as a jet and removed from the proto-jet list. Otherwise, the transverse energy shared with the highest E_{T} neighbor proto-jet is compared to the total transverse energy of this neighbor proto-jet. If the fraction is greater than f (typically 50%) the proto-jets are merged, otherwise the shared objects are individually assigned to the proto-jet that is closest in η,ϕ space. The procedure is repeated, again always starting with the highest E_{T} proto-jet, until no proto-jets are left. This algorithm implements the energy scheme to calculate the proto-jet properties but a different recombination scheme may be used for the final jet. The parameters of the algorithm include a seed threshold, a cone radius, a threshold f on the shared energy fraction for jet merging, and also a maximum number of proto-jets that are used to calculate midpoints.

11.2.3 Inclusive k_{T} algorithm

The inclusive k_{T} jet algorithm is a cluster-based jet algorithm. The cluster procedure starts with a list of input objects, stable particles or calorimeter cells. For each object i and each pair (i, j) the following distances are calculated:

$$\begin{aligned} d_i &= (E_{\mathrm{T},i})^2 R^2, \\ d_{ij} &= \min\{E^2_{\mathrm{T},i}\,,\, E^2_{\mathrm{T},j}\} R^2_{ij} \quad \text{with} \quad R^2_{ij} = (\eta_i - \eta_j)^2 + (\phi_i - \phi_j)^2, \end{aligned}$$

where R^2 is a dimensionless parameter normally set to unity [261]. The algorithm searches for the smallest d_i or d_{ij}. If a value of type d_{ij} is the smallest, the corresponding objects i and j are removed from the list of input objects. They are merged using one of the recombination schemes listed below and filled as one new object into the list of input objects. If a distance of type d_i is the smallest, then the corresponding object i is removed from the list of input

objects and filled into the list of final jets. The procedure is repeated until all objects are included in jets. The algorithm successively merges objects which have a distance $R_{ij} < R$. It follows that $R_{ij} > R$ for all final jets i and j.

11.3 Monte Carlo corrections

The jet response was studied with fully simulated QCD dijet events over the range $0 < \hat{p}_{\mathrm{T}} < 4000$ GeV/c [264]. Jets were reconstructed using the iterative cone algorithm ($R = 0.5$), midpoint cone, and cluster-based k_{T} techniques using the E_{T} scheme. Comparisons between Monte Carlo simulation particle-level and reconstructed jets were made by applying the same jet algorithm to stable particles (excluding neutrinos and muons) and calorimeter cells, respectively. A matching criterion, based on the distance $\Delta R = \sqrt{\Delta\eta^2 + \Delta\phi^2} < 0.2$, was used to associate Monte Carlo particle-level and reconstructed jets.

The data were divided into η bins where the ratio of reconstructed jet transverse energy ($E_{\mathrm{T}}^{\mathrm{rec}}$) to the Monte Carlo particle-level jet transverse energy ($E_{\mathrm{T}}^{\mathrm{MC}}$), as a function of $E_{\mathrm{T}}^{\mathrm{MC}}$ was fit using an iterative procedure [264]. Figure 11.4 shows the ratio R_{jet} as a function of pseudorapidity for different generated jet p_{T} before Monte Carlo corrections.

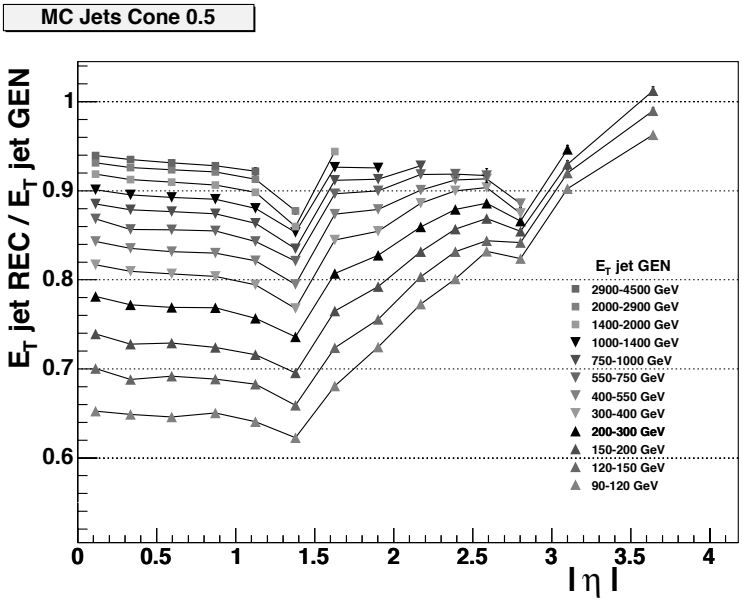

Figure 11.4: The ratio of the reconstructed jet transverse energy $E_{\mathrm{T}}^{\mathrm{rec}}$ to the generated transverse energy $E_{\mathrm{T}}^{\mathrm{MC}}$ as a function of generated jet η for jets with different $E_{\mathrm{T}}^{\mathrm{MC}}$ reconstructed by the iterative cone $R = 0.5$ algorithm before Monte Carlo corrections.

11.4 Jet resolution

The jet resolution was determined from a sample of QCD dijet events with parton transverse momenta ($\hat{p}_{\mathrm{T}}$) in the range 0–4000 GeV/c generated with PYTHIA (version 6.226). The events were fully simulated, digitized, and reconstructed assuming low luminosity conditions ($\mathcal{L} = 2 \times 10^{33}\mathrm{cm}^{-2}\mathrm{s}^{-1}$) [265]. The events were divided into 21 bins of $\hat{p}_{\mathrm{T}}$ with a statis-

tics of 10^4 events per $\hat{p}_{\mathrm{T}}$ bin. All jets reconstructed in these events are included in the resolution fits. For the purpose of evaluating the linearity of the jet response, particle-level jets were reconstructed from all stable particles (excluding neutrinos and muons) using all 3 jet algorithms: the iterative cone algorithm with a cone size $R = 0.5$, the cluster-based k_{T} algorithm, and the midpoint-cone algorithm. The E_{T} recombination scheme was used. The particle-level jets are required to have $|\eta| < 5$, corresponding to the full η coverage of the calorimeters. A matching criterion based on the distance $R = 0.2$ in η, ϕ space was used to associate particle-level and reconstructed jets axes.

The reconstructed jet transverse energy ($E_{\mathrm{T}}^{\mathrm{rec}}$) was compared to the MC generated transverse energy ($E_{\mathrm{T}}^{\mathrm{MC}}$). The distribution of $E_{\mathrm{T}}^{\mathrm{rec}}/E_{\mathrm{T}}^{\mathrm{MC}}$ was fit to obtain the resolution as shown in Figure 11.5. The lower value of $E_{\mathrm{T}}^{\mathrm{rec}}$ compared to $E_{\mathrm{T}}^{\mathrm{MC}}$ is due in part to the fact that the ECAL is calibrated on photons, whereas a substantial amount of jet energy deposited in the ECAL arises from charged pions. For the lowest energy jets, the distribution of of $E_{\mathrm{T}}^{\mathrm{rec}}/E_{\mathrm{T}}^{\mathrm{MC}}$ is asymmetric and a fit is done in the vicinity of the peak position. The results of these fits provide an MC jet correction function that may be applied to reconstructed jets.

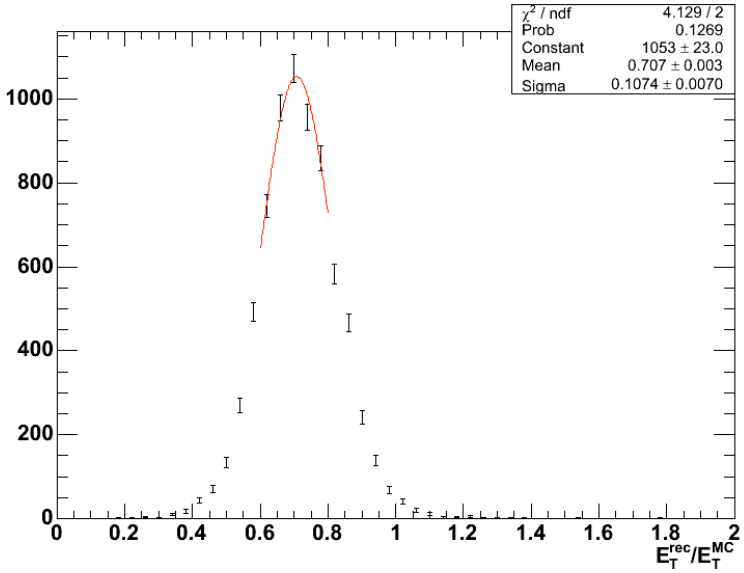

Figure 11.5: Distribution of reconstructed jet transverse energy ($E_{\mathrm{T}}^{\mathrm{rec}} = p_{\mathrm{T}}^{\mathrm{rec}}c$) divided by particle-level generated jet transverse energy ($E_{\mathrm{T}}^{\mathrm{MC}} = p_{\mathrm{T}}^{\mathrm{MC}}c$) for generated jets in the range $105\,\mathrm{GeV} < E_{\mathrm{T}}^{\mathrm{MC}} < 115\,\mathrm{GeV}$. The jets are reconstructed with the iterative cone $R = 0.5$ algorithm.

The resolution plots were fitted with the following functional form:

$$\frac{\sigma\left(\frac{E_{\mathrm{T}}^{\mathrm{rec}}}{E_{\mathrm{T}}^{\mathrm{MC}}}\right)}{\langle\frac{E_{\mathrm{T}}^{\mathrm{rec}}}{E_{\mathrm{T}}^{\mathrm{MC}}}\rangle} = \frac{a}{E_{\mathrm{T}}^{\mathrm{MC}}} \oplus \frac{b}{\sqrt{E_{\mathrm{T}}^{\mathrm{MC}}}} \oplus c \tag{11.1}$$

where the first term is due to fixed energy fluctuations in the cone from electronics noise, pile-up and underlying event energy, the second term comes from the stochastic response of the calorimeter measurements and the last term is the constant term from residual non-

uniformities and non-linearities in the detector response. The fits were done down to a transverse energies of 30 GeV in the barrel and endcap and 20 GeV in the forward region.

The resulting jet resolution for jets with $|\eta| < 1.4$ reconstructed with the iterative cone $R = 0.5$ algorithm is shown in Figure 11.6. The resolution curves for the barrel, endcap and forward regions are shown in Figure 11.7. The resolution curves on the measurement of ϕ and η of the jets for the barrel, endcap and very forward regions are shown in Figs. 11.8 and 11.9.

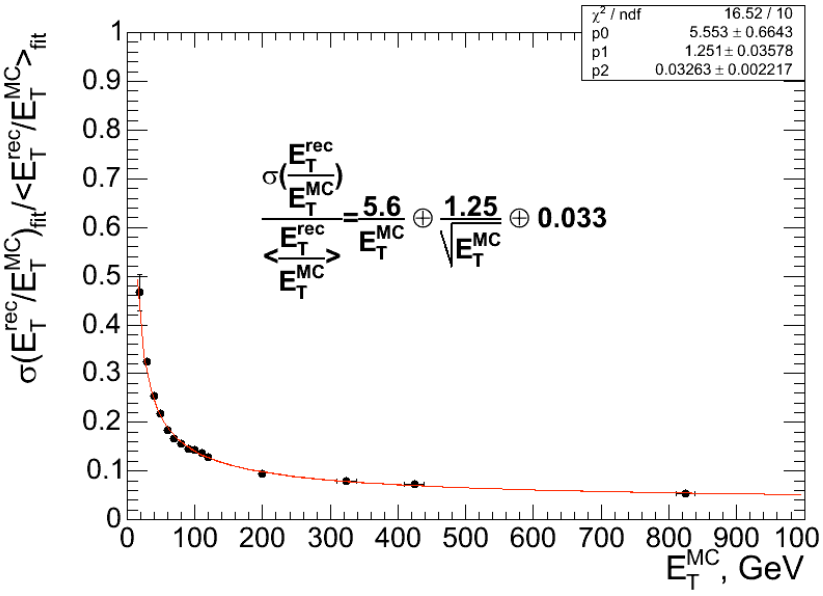

Figure 11.6: The jet transverse energy resolution as a function of the generated jet transverse energy for barrel jets ($|\eta| < 1.4$). The cuts $E_{\mathrm{T}} > 0.5$ GeV and $E > 0.8$ GeV are used. The distance between generated and reconstructed jets is $\Delta R < 0.2$. The Monte Carlo jet calibration has been applied.

11.5 Missing transverse energy

Beginning with UA1 [266], all major detectors at hadron colliders have been designed to cover as much solid angle as practically possible with calorimetry [3]. The primary motivation of this is to provide as complete of a picture as possible of the event, including the presence of one or more energetic neutrinos or other weakly-interacting stable particles though apparent missing energy. Energetic particles produced in the direction of the beam pipe make it impossible to directly measure missing energy longitudinal to the beam direction, however, the transverse energy balance can be measured with an accuracy good enough to help establish a physics signature involving one or more non-interacting particles. The W boson was discovered and its mass determined to 3% with just 6 events due to the ability of UA1 to infer the presence of 40 GeV neutrinos with a resolution of a few GeV [267]. Since the time of the W discovery, measurement of missing transverse energy has been a major tool in the search for new phenomena at hadron colliders [268]–[273].

Measurement of missing transverse energy vector ($\mathbf{E}_{\mathrm{T}}^{\mathrm{miss}}$) at the LHC will be complicated by the presence of pile-up collisions. In CMS, measurement of $\mathbf{E}_{\mathrm{T}}^{\mathrm{miss}}$ will be further degraded by

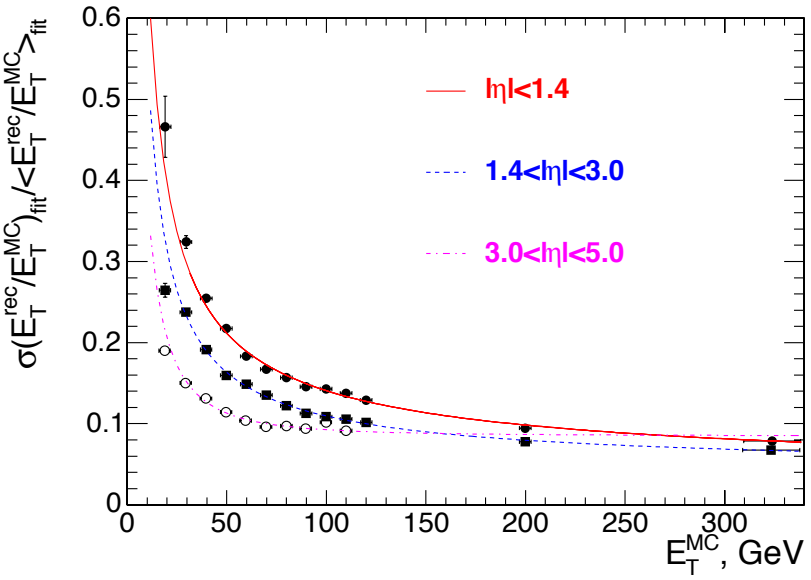

Figure 11.7: The jet transverse energy resolution as a function of the generated jet transverse energy for barrel jets ($|\eta| < 1.4$), endcap jets ($1.4 < |\eta| < 3.0$) and very forward jets ($3.0 < |\eta| < 5.0$). The jets are reconstructed with the iterative cone $R = 0.5$ algorithm. The cuts $E_{\mathrm{T}} > 0.5$ GeV and $E > 0.8$ GeV are used. The distance between generated and reconstructed jets is required to be $\Delta R < 0.2$. The Monte Carlo jet calibration has been applied.

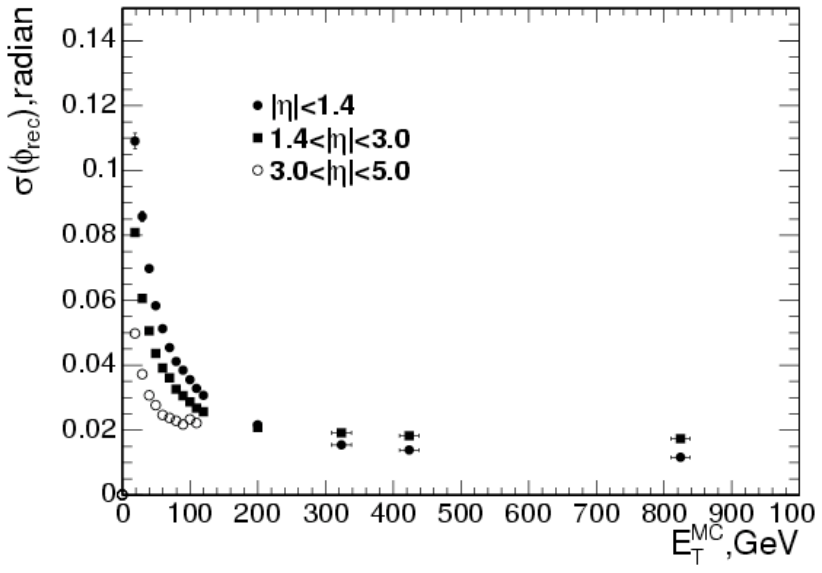

Figure 11.8: The jet ϕ angular resolution as a function of the generated jet transverse energy for barrel jets ($|\eta| < 1.4$), endcap jets ($1.4 < |\eta| < 3.0$) and very forward jets ($3.0 < |\eta| < 5.0$). The cuts $E_{\mathrm{T}} > 0.5$ GeV and $E > 0.8$ GeV are used. The distance between generated and reconstructed jets is required to be $\Delta R < 0.2$.

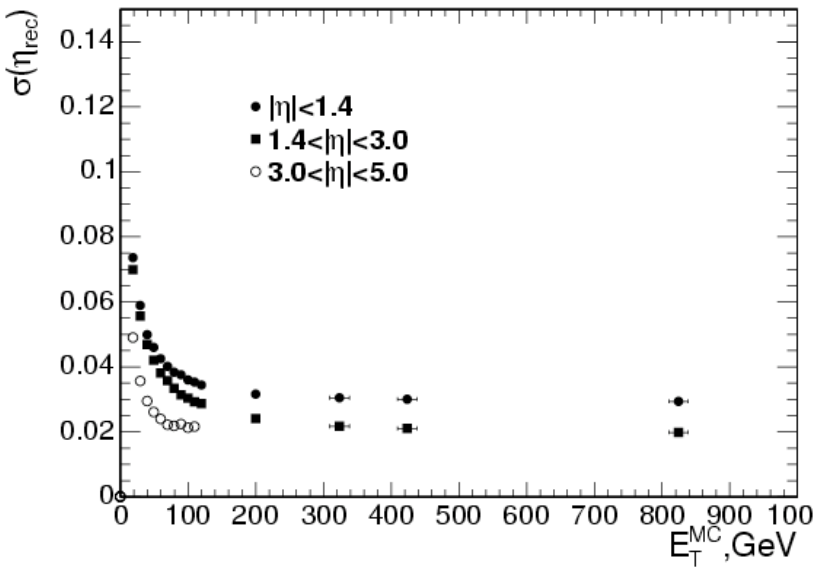

Figure 11.9: The jet η resolution as a function of the generated jet transverse energy for barrel jets ($|\eta| < 1.4$), endcap jets ($1.4 < |\eta| < 3.0$) and very forward jets ($3.0 < |\eta| < 5.0$). The cuts $E_{\mathrm{T}} > 0.5$ GeV and $E > 0.8$ GeV are used. The distance between generated and reconstructed jets is required to be $\Delta R < 0.2$.

the difference between photon and pion response in the combined ECAL plus HCAL detectors and by the bending of tracks by the 4 T magnetic field. On the other hand, the excellent cell segmentation, hermeticity, and good forward coverage of CMS will help measurement of $\mathbf{E}_{\mathrm{T}}^{\mathrm{miss}}$. In spite of all these detector subtleties, the $\mathbf{E}_{\mathrm{T}}^{\mathrm{miss}}$ resolution in CMS is expected to be dominated by calorimeter resolution as discussed in Section 11.4 [274].

11.5.1 Comparison with UA1 and CDF

The missing transverse energy vector is calculated by summing individual calorimeter towers having energy E_n, polar angle θ_n and azimuthal angle ϕ_n:

$$\mathbf{E}_{\mathrm{T}}^{\mathrm{miss}} = \Sigma(E_n \sin\theta_n \cos\phi_n \hat{\mathbf{i}} + E_n \sin\theta_n \sin\phi_n \hat{\mathbf{j}}) = E_x^{\mathrm{miss}} \hat{\mathbf{i}} + E_y^{\mathrm{miss}} \hat{\mathbf{j}} \,.$$

Reconstructed muons are taken into account by replacing the expected calorimeter deposit (about 4 GeV) with the reconstructed track p_{T}. It was observed in UA1 that the $E_{\mathrm{T}}^{\mathrm{miss}}$ resolution was dependent on the overall activity of the event, characterized by the scalar sum of transverse energy in all calorimeter cells (ΣE_{T}). The resolution is observed to follow the form $\sigma = C\sqrt{\Sigma E_{\mathrm{T}}}$ GeV$^{1/2}$ where C is a constant that depends directly on the calorimeter jet resolution and ΣE_{T} is the scalar sum of the transverse energy of all calorimeter hits. For UA1, the calorimeter (jet) resolution was approximately $0.8\sqrt{E_{\mathrm{T}}}$ GeV$^{1/2}$ which let to an observed distribution of x- or y- components, E_x^{miss} or E_y^{miss}, in minimum bias events that was Gaussian with zero mean and standard deviation $\sigma_x = \sigma_y = 0.4\sqrt{\Sigma E_{\mathrm{T}}}$ GeV$^{1/2}$ [267]. The CDF experiment, which has a scintillating tile geometry similar to CMS (and a completely different magnetic field configuration compared to UA1, solenoid vs. dipole), observed $\sigma_x = 0.47\sqrt{\Sigma E_{\mathrm{T}}}$ GeV$^{1/2}$ in Run I [275]. From the UA1 and CDF results and the CMS

jet resolution ($1.25\sqrt{E_{\rm T}}$ GeV$^{1/2}$) explained in Section 11.4, one may expect an $E_{\rm T}^{\rm miss}$ resolution in CMS of $\sigma_x \approx (0.6-0.7)\sqrt{\Sigma E_{\rm T}}$ GeV$^{1/2}$ for minimum bias events with no pile-up, when dominated by the shower fluctuations and not electronic noise [274].

11.5.2 Resolution in minimum bias events

Figure 11.10 shows the Monte Carlo simulation distributions of $\Sigma E_{\rm T}$ and $E_x^{\rm miss}$ expected in CMS from a high statistics sample of fully reconstructed minimum bias events. In order to compare the CMS result to what may be expected from previous experiments, it is essential to separate out the stochastic part from the electronic noise, the latter of which can greatly effect the observed $\Sigma E_{\rm T}$. For a given set of calorimeter thresholds, there corresponds an offset, i.e., a minimum value of $\Sigma E_{\rm T}$ that will be recorded, which may be seen to be about 150 GeV in Fig. 11.10. The $E_{\rm T}^{\rm miss}$ resolution shown in Fig. 11.10 is 6.1 GeV in excellent agreement with expectations based on a stochastic contribution of 4.8 GeV from calorimeter resolution and 3.8 GeV from electronic noise. It is important to note that at this stage, we are forming the vector $\mathbf{E}_{\rm T}^{\rm miss} = E_x\hat{\mathbf{i}} + E_y\hat{\mathbf{j}}$ using ECAL cells calibrated for photons and HCAL cells calibration for hadrons, appropriate perhaps for understanding the detector response to first collisions. It is believed that making use of energy flow techniques such as the charged track corrections described in Section 11.8 will ultimately improve the $\mathbf{E}_{\rm T}^{\rm miss}$ resolution.

11.5.3 Missing transverse energy resolution in QCD events

While the minimum bias events provide a good check for understanding the calorimeters, a major background to any potential signal containing missing transverse energy will come from QCD. The observed $\mathbf{E}_{\rm T}^{\rm miss}$ resolution is degraded in the presence of event pile-up which results in an increase of overall activity observed in the calorimeters. Even at low luminosity ($\mathcal{L} = 2 \times 10^{33}{\rm cm}^{-2}{\rm s}^{-1}$), there will be an average of 3.5 fully inelastic pile-up events per 25 ns beam crossing (5.0 events including diffractive processes). To study the detector $\mathbf{E}_{\rm T}^{\rm miss}$ resolution in events with hard collisions, 3×10^6 QCD events were generated and fully reconstructed. The events correspond to parton transverse momenta ($\hat{p}_{\rm T}$) ranging from 0–4000 GeV/c. The QCD events were all generated with low luminosity pile-up.

The QCD events with the softest collisions, $0 < \hat{p}_{\rm T} < 15$ GeV, were used to make a connection with the resolution studies performed with the minimum bias sample. Figure 11.11 shows the observed $\Sigma E_{\rm T}$ and $E_x^{\rm miss}$ distributions in these soft QCD events. The observed missing transverse energy resolution of 9.9 GeV is comparable to that from minimum bias events with the addition of pile-up.

Figure 11.12 shows the reconstructed $E_{\rm T}^{\rm miss}$ resolution vs. observed $\Sigma E_{\rm T}$ for both minimum bias events (open circles) and soft QCD events having $0 < \hat{p}_{\rm T} < 15$ GeV/c (squares). Low-luminosity pile-up is included in both cases. In the region of overlap between the minimum bias and soft QCD samples (near $\Sigma E_{\rm T}$ = 250 GeV), the reconstructed transverse energy balance is in excellent agreement.

The reconstructed $\Sigma E_{\rm T}$ for QCD events is shown in Fig. 11.13. The value of $\Sigma E_{\rm T}$ is seen to range from about 500 GeV at $\hat{p}_{\rm T} \approx 65$ GeV/c to 1 TeV at $\hat{p}_{\rm T} \approx 340$ GeV/c to 1.7 TeV at $\hat{p}_{\rm T} \approx 700$ GeV/c. It is well known that $\mathbf{E}_{\rm T}^{\rm miss}$ resolution degrades in very active events compared to the ideal case of minimum bias events; for example, the average reconstructed missing transverse energy observed in UA1 jet events was $\langle E_{\rm T}^{\rm miss}\rangle = 0.7\sqrt{\Sigma E_{\rm T}}$ GeV$^{1/2}$ [268]

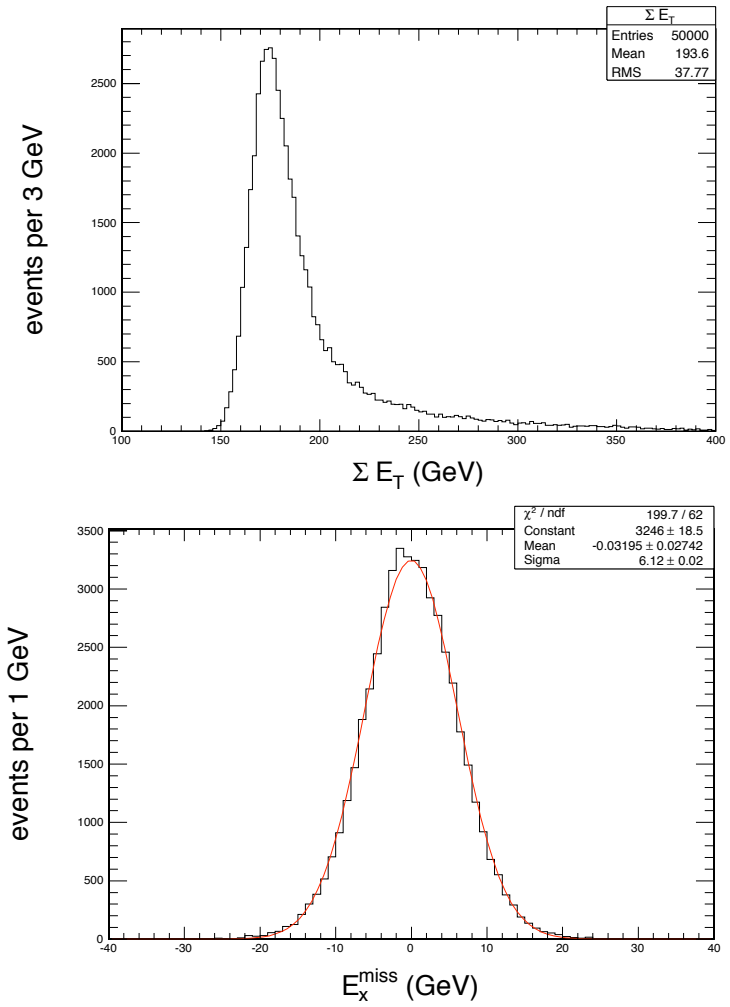

Figure 11.10: Top) Distribution of ΣE_{T} and Bottom) E_x^{miss} for minimum bias events with no pile-up. The resolution is 6.1 GeV in agreement with expectations based on a stochastic term of $0.65\sqrt{\Sigma E_{\mathrm{T}}}$ GeV$^{1/2}$ and a noise contribution of 3.8 GeV.

about 25% more than observed in minimum bias when scaled with ΣE_{T}. In hard-scatter QCD events, the distributions of E_x are also no longer perfectly Gaussian. In this case, the standard deviation of the E_x^{miss} distribution is used as the measure of resolution. Figure 11.14 shows the resolution for QCD events as a function of reconstructed ΣE_{T}. Note the agreement at ΣE_{T} = 500 GeV with Fig. 11.12 which gave $\sigma_x \approx 12$ GeV. The resolution at larger values of ΣE_{T}, however, follows a steeper path which approximately scales from the UA1 result. A fit to the resolution gives $\sigma^2 = (3.8\ \mathrm{GeV})^2 + (0.97\ \mathrm{GeV}^{1/2})^2 \Sigma E_{\mathrm{T}} + (0.012 \Sigma E_{\mathrm{T}})^2$.

The observed $E_{\mathrm{T}}^{\mathrm{miss}}$ balance is directly related to the $E_{\mathrm{T}}^{\mathrm{miss}}$ resolution. The observed $E_{\mathrm{T}}^{\mathrm{miss}}$ distribution, of course, by its construction has a one-sided tail. A small $\hat{p}_{\mathrm{T}}$ interval can create a wide spectrum of $E_{\mathrm{T}}^{\mathrm{miss}}$ at both generator and detector level. The reconstructed $E_{\mathrm{T}}^{\mathrm{miss}}$ for different intervals of parton-level generator $\hat{p}_{\mathrm{T}}$ are shown in Fig. 11.15. The reconstructed $E_{\mathrm{T}}^{\mathrm{miss}}$ in QCD events (with pile-up) is shown in Fig. 11.16. At ΣE_{T} = 1700 GeV, which corresponds to $p_{\mathrm{T}} \approx 700$ GeV/c jets, an average $E_{\mathrm{T}}^{\mathrm{miss}}$ of about 50 GeV is observed. This number is consistent with measurement of such jets with a resolution of $1.25\ \mathrm{GeV}^{1/2}\sqrt{E_{\mathrm{T}}}$. A fit to the reconstructed missing transverse energy gives $(E_{\mathrm{T}}^{\mathrm{miss}})^2 = (5.4\ \mathrm{GeV})^2 + (1.23\ \mathrm{GeV}^{1/2})^2 \Sigma E_{\mathrm{T}} +$

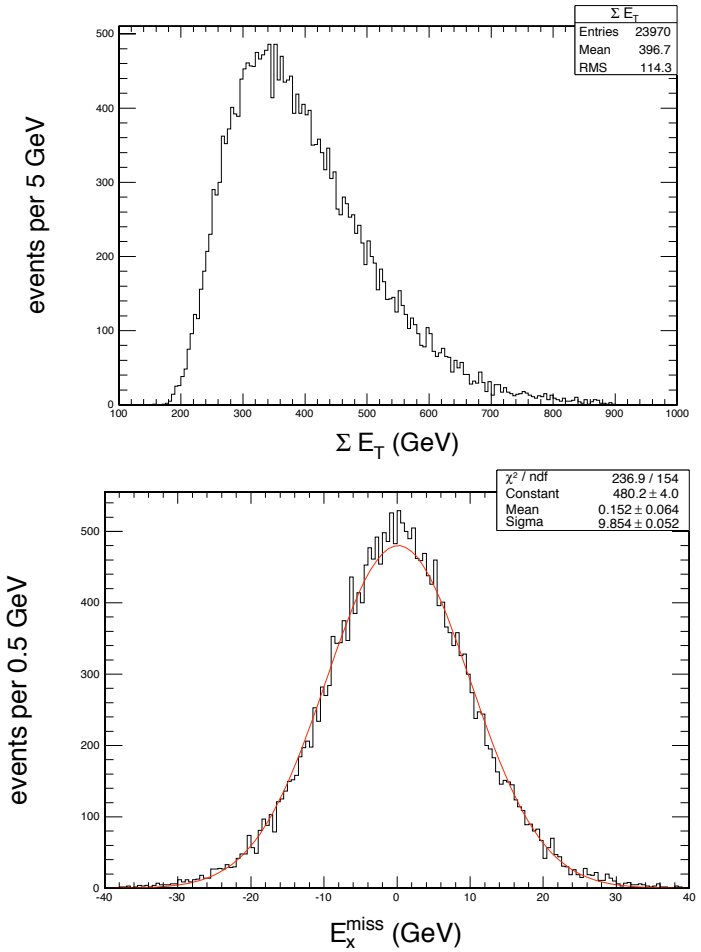

Figure 11.11: Top) Distribution of $\Sigma E_{\rm T}$ and Bottom) $E_x^{\rm miss}$ for soft QCD events ($0 < \hat{p}_{\rm T} < 15{\rm GeV}$) with pile-up. The resolution is 9.9 GeV in agreement with expectations based the study with minimum bias events.

$(0.019\Sigma E_{\rm T})^2$.

As an additional check of detector $\mathbf{E}_{\rm T}^{\rm miss}$ performance, one may look at the resolution in a direction orthogonal to the jet axis. By choosing this direction, the observed resolution is independent of the reconstructed jet resolution, but rather is dominated by the underlying event and pile-up activity. This distribution is shown in Fig. 11.17 vs. $\Sigma E_{\rm T}$. Once again, as expected, the resolution is comparable to that observed in soft collisions (Fig. 11.11). It is believed that the jet calibration described in the following section will serve as the basis for more sophisticated $\mathbf{E}_{\rm T}^{\rm miss}$ corrections and that ultimately energy flow techniques that account for calorimeter nonlinearities, magnetic field, and good charged particle resolution from the tracker can improve $\mathbf{E}_{\rm T}^{\rm miss}$ resolution.

11.5.4 Corrections to $\mathbf{E}_{\rm T}^{\rm miss}$

For QCD events, where reconstructed $\mathbf{E}_{\rm T}^{\rm miss}$ is largely an artifact of detector response, it is observed that correcting the jet energies (as described in the next section) does not significantly improve the missing transverse energy resolution except in the case where the leading jets have significantly different rapidities (and thus, much different energies). In events which

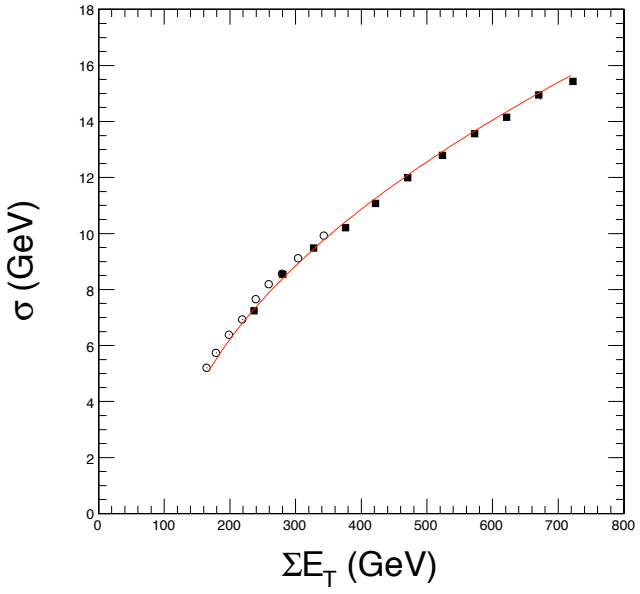

Figure 11.12: Missing transverse energy resolution vs. ΣE_{T} for QCD soft events, $0 < \hat{p}_{\mathrm{T}} < 15\ \mathrm{GeV}/c$, (squares) and minimum bias events (open circles). Low-luminosity pile-up is included in both cases.

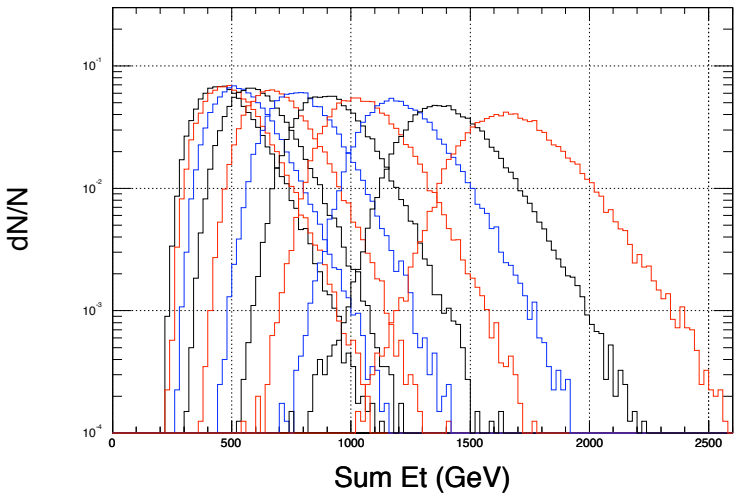

Figure 11.13: Distribution of ΣE_{T} observed in the detector for QCD events corresponding to $\hat{p}_{\mathrm{T}}$ ranges (from left to right) of 20-30, 30-50, 50-80, 80-120, 120-170, 170-230, 230-300, 300-380, 380-470, 470-600 and 600-800 GeV/c.

have a large true $\mathbf{E}_{\mathrm{T}}^{\mathrm{miss}}$, its reconstruction is underestimated due to nonlinearity of the calorimeter. In this case, a jet energy correction serves to help calibrate (linearize) the missing transverse energy scale [274].

A sample of $t\bar{t}$ events was used to investigate a number of corrections to measurement of $\mathbf{E}_{\mathrm{T}}^{\mathrm{miss}}$ in events with one or more energetic neutrinos (i.e., genuine $\mathbf{E}_{\mathrm{T}}^{\mathrm{miss}}$). Figure 11.18 shows the resolution before and after jet corrections for inclusive $t\bar{t}$ events vs. reconstructed $E_{\mathrm{T}}^{\mathrm{miss}}$. For large values of reconstructed $E_{\mathrm{T}}^{\mathrm{miss}}$, we observe an improvement in resolution of nearly

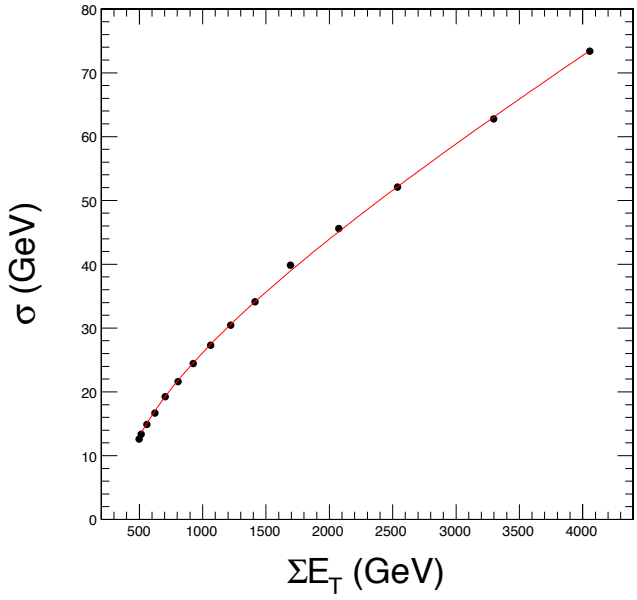

Figure 11.14: Missing transverse energy resolution vs. ΣE_{T} for QCD events with pile-up. The fit gives a stochastic contribution of $0.97\sqrt{\Sigma E_{\mathrm{T}}}$.

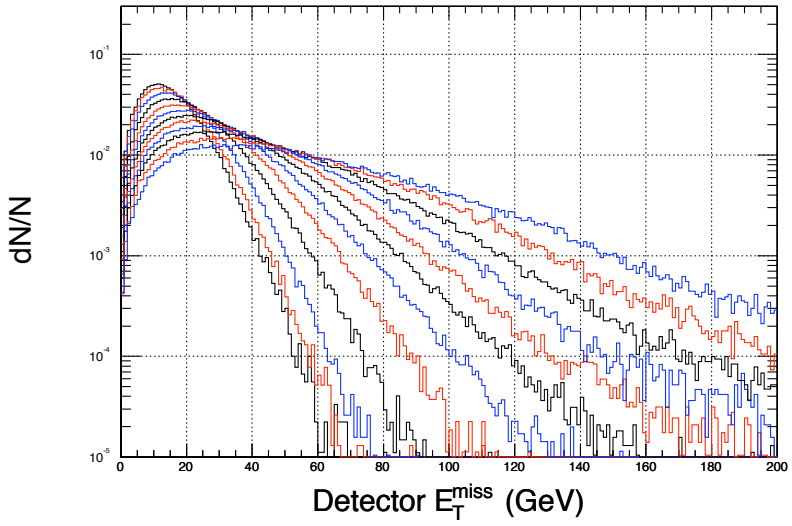

Figure 11.15: Missing transverse energy spectra in QCD samples that correspond to parton-level $\hat{p}_{\mathrm{T}}$ ranges of (from left to right) 20-30, 30-50, 50-80, 80-120, 120-170, 170-230, 230-300, 300-380, 380-470, 470-600, 600-800 and 800-1000 GeV/c.

15%.

Figure 11.18 shows the error in the reconstructed missing transverse energy scale before and after jet corrections for inclusive $t\bar{t}$ events vs. reconstructed reconstructed $E_{\mathrm{T}}^{\mathrm{miss}}$. As anticipated, the jet corrections (by design) also bring back the true missing transverse energy scale by correcting for calorimeter particle response.

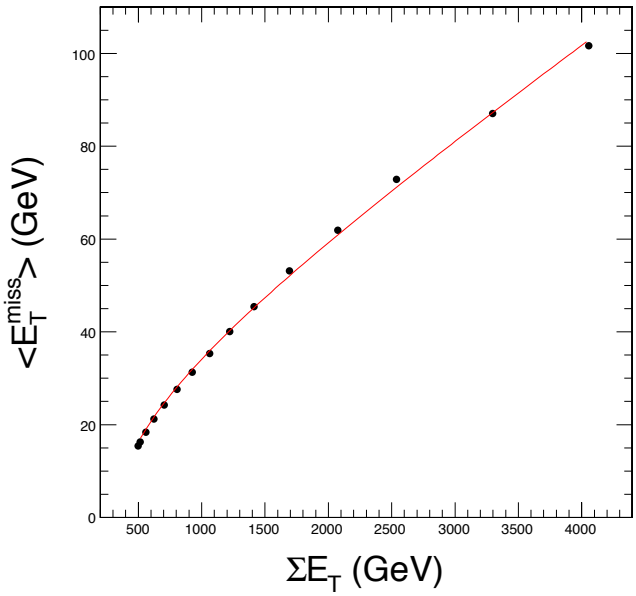

Figure 11.16: Average reconstructed $E_{\mathrm{T}}^{\mathrm{miss}}$ vs. ΣE_{T} for QCD events with pile-up. The fit gives a stochastic contribution of $1.23\sqrt{\Sigma E_{\mathrm{T}}}$.

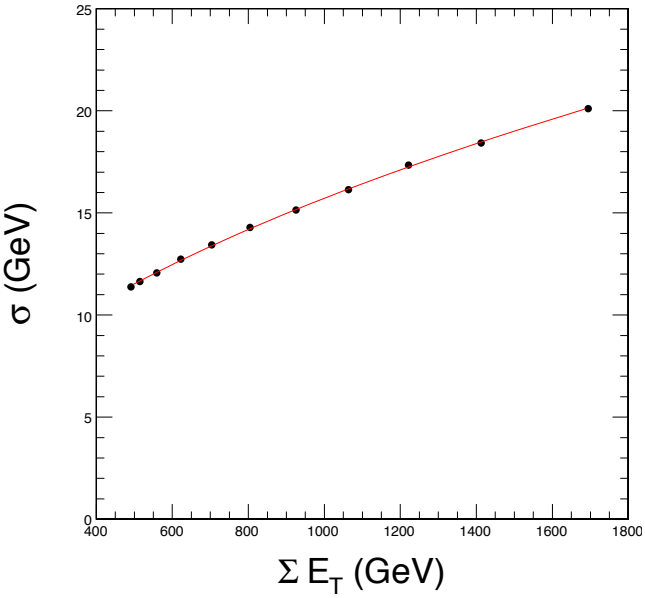

Figure 11.17: Missing transverse energy resolution in a direction orthogonal to the jet axis vs. ΣE_{T} of the entire event. The resolution is comparable to that observed in soft collisions.

11.5.5 Angular resolution

Figure 11.20 shows the angular resolution (ϕ) of the reconstructed missing transverse energy direction from inclusive $t\bar{t}$ events as a function of reconstructed $E_{\mathrm{T}}^{\mathrm{miss}}$, before and after the corrections described in Section 11.5.4. One may see that for low values of $E_{\mathrm{T}}^{\mathrm{miss}}$, the angular resolution is comparable to jet size, while for larger values of $E_{\mathrm{T}}^{\mathrm{miss}}$ the angular resolution approaches that of the calorimeter tower size.

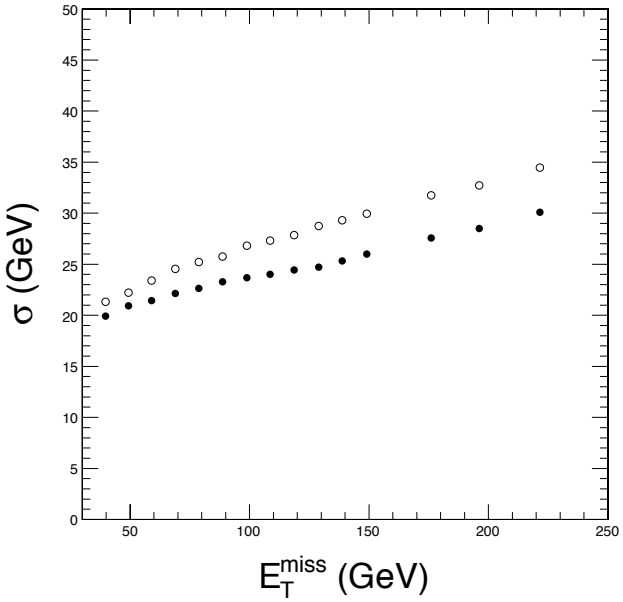

Figure 11.18: Missing transverse energy resolution before (open circles) and after jet corrections (filled circles) for inclusive $t\bar{t}$ events vs. reconstructed $E_{\mathrm{T}}^{\mathrm{miss}}$.

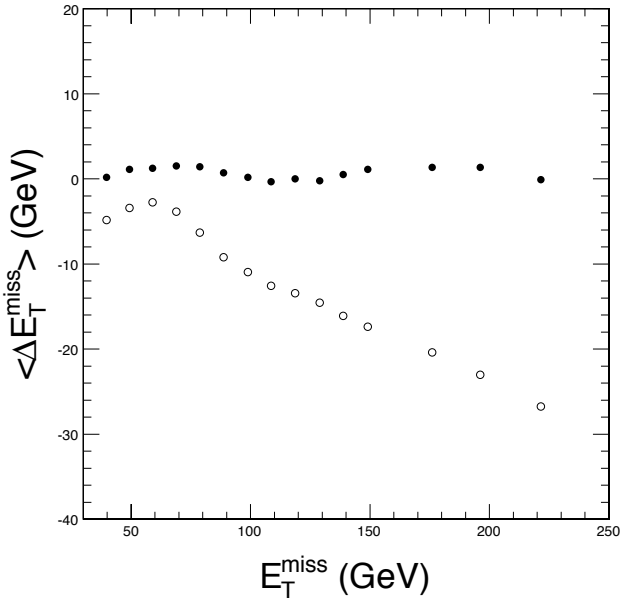

Figure 11.19: Error in the reconstructed missing transverse energy scale before (open circles) and after jet corrections (filled circles) for inclusive $t\bar{t}$ events vs. reconstructed $E_{\mathrm{T}}^{\mathrm{miss}}$.

11.6 Jet calibration

Jet calibration takes place in 2 steps: 1) a reconstructed jet is corrected to particle-level and 2) the particle-level jet is corrected to parton-level, depending on the parton type assumed in the analysis. The particle-level calibration corrects the reconstructed jet energy to equal the energy of particles in a jet from the hard scatter, independently clustered by the same algorithm and matched to the reconstructed jet. The parton-level calibration corrects the

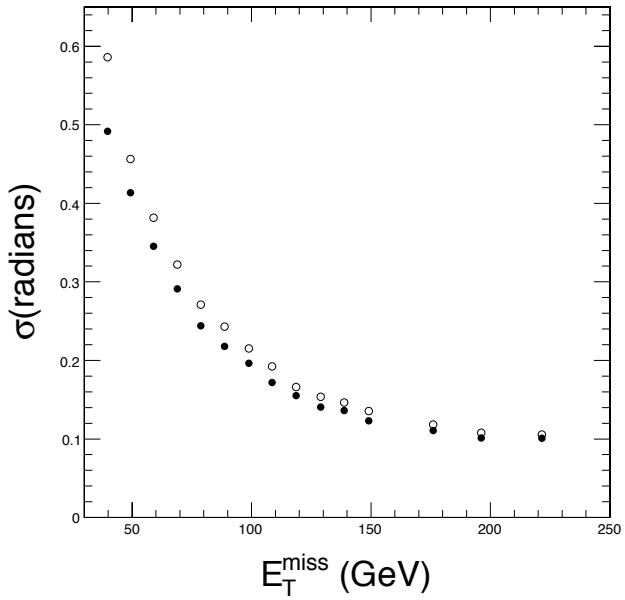

Figure 11.20: Error in the direction of the vector $\mathbf{E}_{\mathrm{T}}^{\mathrm{miss}}$ as a function of reconstructed $E_{\mathrm{T}}^{\mathrm{miss}}$ in inclusive $t\bar{t}$ events before (open circles) and after corrections (filled circles).

energy of a particle-level corrected jet to the energy of the parton that originated the jet. Both steps may be combined into a single correction from the reconstructed jet to the parton-level jet (Section 11.6.3).

The particle-level calibration has 2 components: offset and response. The offset component results from multiple interactions in the event's bunch crossing, pile-up from interactions from neighboring bunch crossings, the underlying event, and any residual electronic noise after calorimeter thresholds are applied. The particle-level calibration subtracts the average offset from the reconstructed jet. The response component results from nonlinear response of the calorimeter to hadrons, differences in response among the calorimeter regions in η, lower response of cracks between calorimeters, and from the different particles contributing to the independently clustered particle-level and reconstructed jets due to magnetic field and shower spreading effects. The particle-level calibration corrects a reconstructed jet at a given p_{T} and η to the average equivalent particle-level jet.

The parton-level calibration accounts for the particles from the originating parton that are not included in the particle-level jet. This correction depends on the hadronization model used and the type of originating parton.

Jet calibrations needs to be derived for each jet algorithm and set of algorithm parameters and also depend on the p_{T} spectrum of the process. The jet calibration provides an average correction for jets reconstructed under a particular configuration and for a particular process.

11.6.1 Data-driven calibration strategy

The MC calibration technique described in Section 11.4 together with the radioactive source calibration and test beam measurements will provide a starting point for understanding the initial calorimeter calibration. The data, however, will provide a number of invaluable tools which may be used to facilitate the overall calibration procedure [276, 277]. The first stage

of the calibration will check the radioactive source calibration at the tower level, while the second stage will check the calibration of jets.

The following procedures have been identified for verifying the calorimeter tower calibration:

- Measure noise with beam-crossing triggers to check and adjust thresholds.
- Take data without zero-suppression to study the electronic noise offset.
- Check and adjust phi symmetry with minimum bias triggers.
- Use isolated muons from W decays to compare the tower-to-tower response to radioactive source source measurements and test beam muons.
- Compare isolated high p_{T} charged tracks with test beam data.

The following procedures will be used to check the calibration of jets.

- Measure the effect of pile-up on clustering algorithms and thresholds.
- Use p_{T} balance in QCD dijet events as described in Section 11.6.2 to calibrate the jet energy scale vs. η and verify the resolution.
- Use p_{T} balance in γ+jet events as described in Section 11.6.3 to calibrate the absolute energy scale.
- Use W mass fitting in tagged $\mathrm{t\bar{t}}$ events as described in Section 11.6.5 to check and fine tune the jet energy scale.

We expect that a 5% overall uncertainty in the jet energy scale can be achieved before including the W mass fit. The W mass constraint discussed in Section 11.6.5 could reduce this uncertainty to 3% for low p_{T} jets.

11.6.2 Dijet balancing

Transverse momentum balance in QCD dijet events is a proven technique to measure relative jet response and resolution from data. The results can be used to calibrate and test the full CMS simulation.

Events are selected having 1 of the 2 leading jets in the region $|\eta| < 1$ (the "barrel" jet). The other leading jet (the "probe" jet) may be at any value of η. The dijet p_{T} is defined by

$$p_{\mathrm{T}}^{\mathrm{dijet}} = (p_{\mathrm{T}}^{\mathrm{probe}} + p_{\mathrm{T}}^{\mathrm{barrel}})/2,$$

We divide the data into bins of probe jet η and measure the dijet balance (b) defined by

$$b = (p_{\mathrm{T}}^{\mathrm{probe}} - p_{\mathrm{T}}^{\mathrm{barrel}})/p_{\mathrm{T}}^{\mathrm{dijet}}$$

The dijet relative response, defined as the fractional difference between the jet response in the probe region and the jet response for $|\eta| < 1$, is then $2\bar{b}/(2-\bar{b})$, where $\bar{b}$ is the mean value of the dijet balance distribution. The dijet relative response as a function of probe jet η is shown in Figure 11.21. A significant η dependence is expected due to tower geometry and other instrumental effects, however, the distribution flattens when MC corrections are applied.

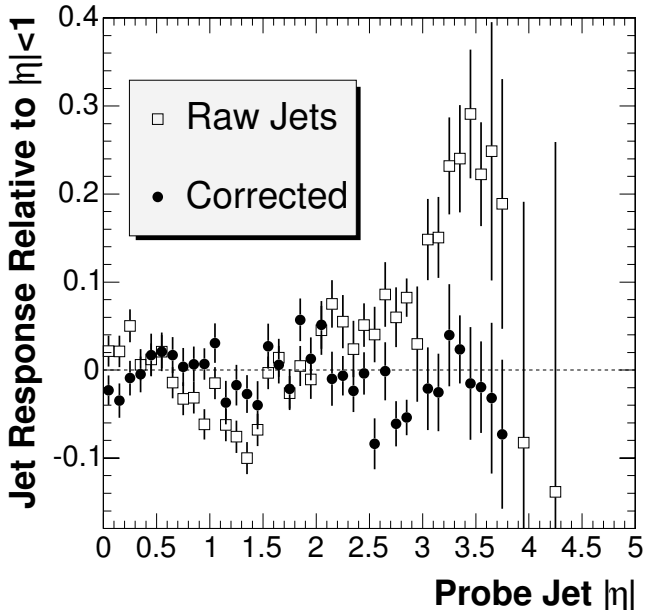

Figure 11.21: Jet response as a function of $|\eta|$ for 120 GeV/c <dijet p_{T} < 250 GeV/c. The graphs compares raw jets (open boxes) with corrected jets (solid circles). The indicated level of precision may be obtained on 1 hour of data taking.

Dijet balancing can be used to derive calibrations as a function of η based solely on the data. The errors shown on the response in Figure 11.21 correspond to a QCD sample of approximately 10^4 events. If an efficient trigger can be deployed for a p_{T} threshold of 120 GeV/c prescaled to an HLT rate of 2.5 Hz, calibration measurements with the precision shown in Figure 11.21 may be made from 1 hour of data taking. One day of data taking would be enough to calibrate the relative response of the detector to jets with a statistical error of 0.5% in the barrel and 2% in the endcap. These data could be further used to monitor the stability of jet response versus η, and provide daily calibrations to HLT triggers that require stable and uniform jet response.

The jet resolution can be measured from the RMS (σ_B) of the dijet balance. Each of the 2 leading jets contributes to the RMS, so the single jet resolution is given by $\sigma_B/\sqrt{2}$. Hard QCD radiation, generally manifested as extra jets in the event, broadens the resolution and creates non-Gaussian tails. We reduce the effects of QCD radiation to negligible levels by selecting events in which there are not any additional jets with $p_{\mathrm{T}} > 0.1 p_{\mathrm{T}}^{\mathrm{dijet}}$. To measure the jet resolution in the barrel we require that both of the leading jets have $|\eta| < 1$. Figure 11.22 shows the barrel jet resolution measured with dijet balancing as a function of dijet p_{T}, which is comparable for both reconstructed jets and corrected jets. The statistics on the measured resolution are what can be expected for 10^5 events in the indicated dijet p_{T} range.

11.6.3 γ+jet events

Apart from higher-order initial-state effects, the direct photon produced from Compton ($qg \rightarrow q + \gamma$) and annihilation ($q\bar{q} \rightarrow g + \gamma$) processes has a transverse momentum that is balanced by the jet. The high resolution (≈1%) of the electromagnetic calorimeter provides an accurate measurement of the photons and is the basis of the jet calibration procedure. The primary

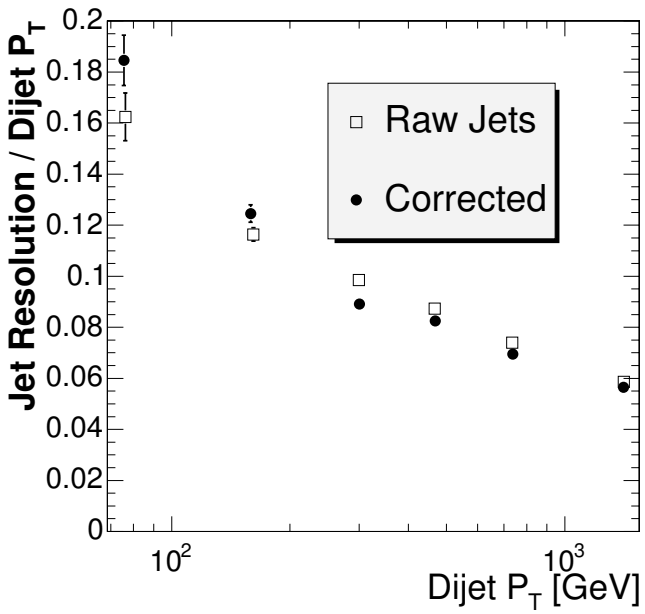

Figure 11.22: Jet resolution for $|\eta| < 1$ as a function of dijet p_{T}.

complications of this calibration procedure come from initial-state radiative corrections and a background of QCD dijet events where one jet is misidentified as a photon in the calorimeter [278].

The measured observable $k_{\mathrm{jet}} \equiv p_{\mathrm{T}}^{jet}/p_{\mathrm{T}}^{\gamma}$ provides an approximate value for the true parton-level calibration of the jet given by $k_{\mathrm{jet}}^{\mathrm{true}} \equiv p_{\mathrm{T}}^{jet}/p_{\mathrm{T}}^{\mathrm{parton}}$. The calibration constant given by $k_{\mathrm{jet}}^{\mathrm{true}}$ is the inverse of the correction factor needed to convert the measured transverse momentum of the jet to the transverse momentum of an initial parton. In the presence of initial state radiation, the transverse momentum balance of the photon and the parton is broken, leading to a two-dimensional distribution in $p_{\mathrm{T}}^{\mathrm{parton}}$ and p_{T}^{γ} (Fig.11.23a). The correlation is symmetric along the line $p_{\mathrm{T}}^{\gamma} = p_{\mathrm{T}}^{\mathrm{parton}}$. Thus the $p_{\mathrm{T}}^{\gamma} - P_{\mathrm{T}}^{\mathrm{parton}}$ balance is preserved by statistically averaging over events with a fixed sum in the transverse momentum of the photon and the parton.

Calibration coefficients are determined directly in bins of p_{T}^{γ}, however, the p_{T} balance of the γ+parton system is broken in this case. From Figure11.23b, projecting a slice of the $p_{\mathrm{T}}^{\mathrm{parton}}$ distribution for p_{T}^{γ} =constant shows a strongly asymmetric distribution with $\langle p_{\mathrm{T}}^{\mathrm{parton}} \rangle < p_{\mathrm{T}}^{\gamma}$. For the measurement of the transverse momentum of the parton, the value k_{jet} will contain an error from initial state radiation corresponding to $\Delta = k_{\mathrm{jet}} - k_{\mathrm{jet}}^{\mathrm{true}} = p_{\mathrm{T}}^{\mathrm{parton}}/p_{\mathrm{T}}^{\gamma} - 1$. This error is significant (6.3% for $p_{\mathrm{T}}^{\gamma} = 100$ GeV), but may be essentially eliminated by defining calibration coefficients k_{jet} to correspond to the peak of the $p_{\mathrm{T}}^{\mathrm{jet}}/p_{\mathrm{T}}^{\gamma}$ spectrum.

Fully simulated γ+jet events are generated with low luminosity ($\mathcal{L} = 2 \times 10^{33}\mathrm{cm}^{-2}\mathrm{s}^{-1}$) and reconstructed using the iterative cone and cluster-based k_T-algorithms. Quantum chromodynamics dijet events in which one jet is misidentified as photon provide the main background to the calibration sample.

The selection of events at the detector level was done with tight cuts on photon isolation ($E_{T\,\gamma}^{\mathrm{isol}} < 5$ GeV), the angle between the photon and the jet ($\Delta\phi_{\gamma,\mathrm{jet}} > 172^{\circ}$) and on transverse

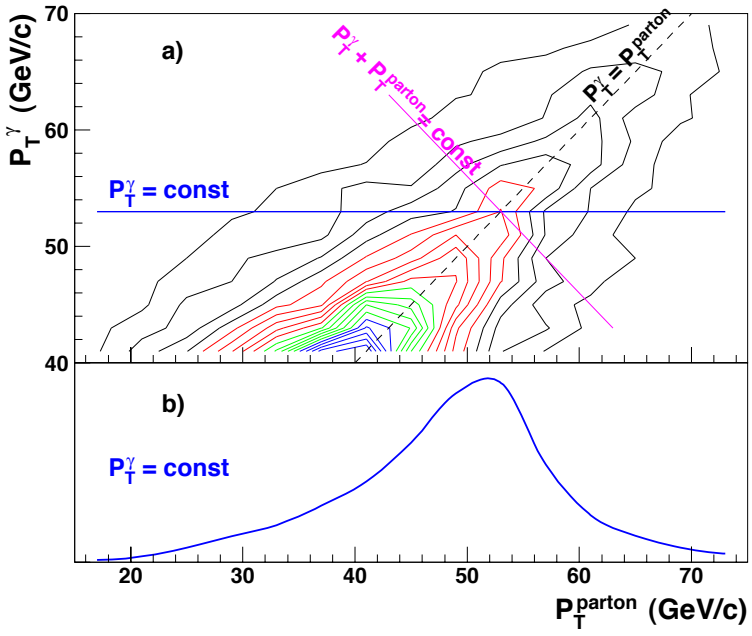

Figure 11.23: a) Distribution of the 2D correlation between the photon and parton transverse momenta, and b) the parton transverse momentum spectrum for a fixed photon transverse momentum in events with direct photons.

energy of additional jets in event ($E_T^{\rm jet2} < 20$ GeV). As a measure of the photon isolation, the value of $E_{T\gamma}^{\rm isol}$ is defined to be the scalar sum of the transverse energy in calorimeter cells within a cone of radius $R = 0.7$ in η, ϕ space with respect to the direction of the parton and outside a central array of 7×7 crystals in the electromagnetic calorimeter. The sum was computed for cells above a threshold of 0.36 and 1.8 GeV for the barrel and endcap of the electromagnetic calorimeters, respectively, and above 2 GeV for the hadron calorimeter. A cut on $E_{T\gamma}^{\rm isol}$ defined in this way gave a large background suppression while maintaining reasonably high signal efficiency(approximately 50%). Figure 11.24 shows signal to background ratio as a function of photon transverse energy. For $E_T^\gamma > 150$ GeV the background is suppressed well below the signal level, while for $E_T^\gamma < 40$ GeV, the background dominates the signal.

Figure 11.25 shows the predicted values for the calibration coefficients and their true values for quark jets and QCD jets, using the iterative cone jet algorithm ($R = 0.5$) and a threshold cut on the transverse energy of calorimeter towers, $E_{\rm T} > 0.5$ GeV. Depending on the algorithm, algorithm parameters and calorimeter cell thresholds, there is a corresponding steepness to the $E_{\rm T}$ dependence of the calibration coefficients and a spread of their values for quark and gluon jets. A strong $E_{\rm T}$ dependence and large spread in response contributes to the error on the calibration.

Figure 11.26 illustrates the sensitivity of calibration errors to the choice of jet algorithm. Quark jets are less sensitive to the jet algorithm compared to gluon jets. For QCD jets, the $k_{\rm T}$ clustering algorithm produces smaller errors than the iterative cone. It should be noted

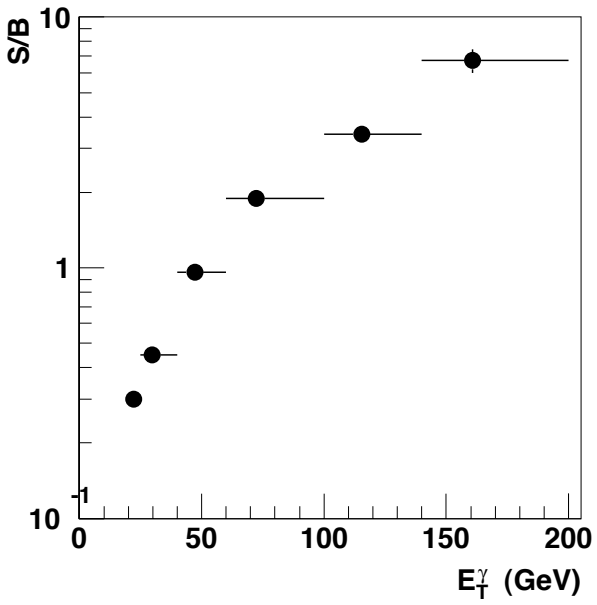

Figure 11.24: The ratio of signal to background after event selection cuts $E_{T\gamma}^{\rm isol} < 5$ GeV, $\Delta\phi_{\gamma,\rm jet} > 172°$, and $E_T^{\rm jet2} < 20$ GeV.

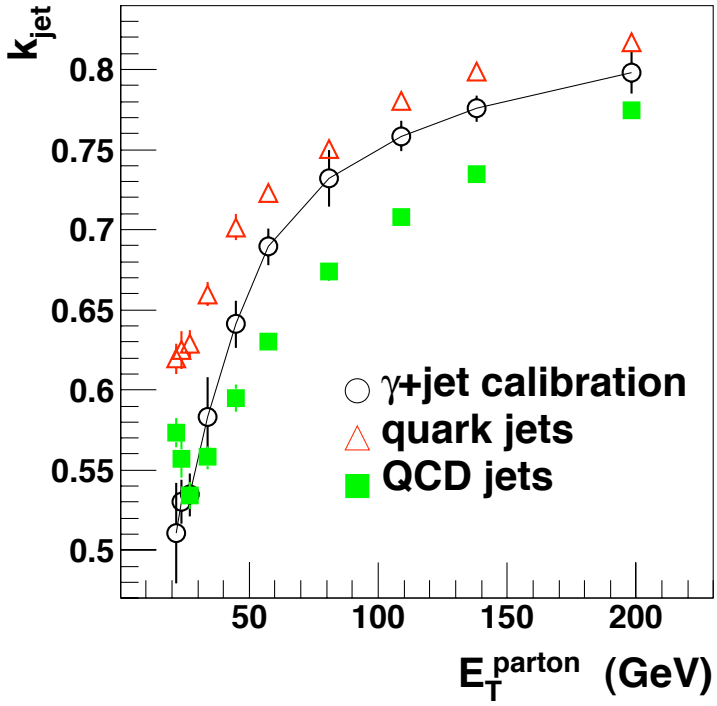

Figure 11.25: The predicted values of calibration coefficients (circles) and their true values for quark (triangles), QCD jet (squares) for the iterative cone algorithm for $|\eta_{\rm jet}| < 1.5$.

that the range of errors on the jet calibration coefficients do not characterize the quality of jet

algorithm. Comparing the effect of thresholds on the calorimeter cell readings, it is found that the lower thresholds yield the most uniform calibration coefficients.

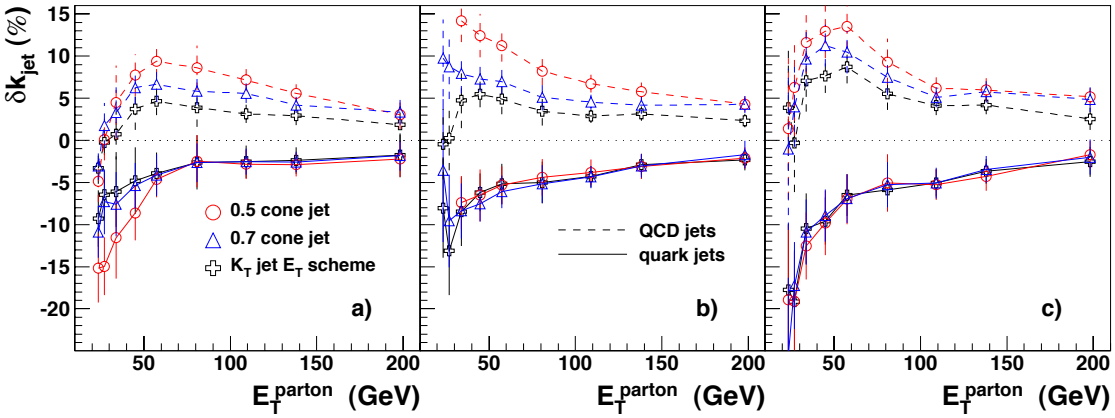

Figure 11.26: Relative systematic errors on the calibration of quark (solid lines) and QCD jets (dashed lines) for the iterative cone algorithm with cone radii of $R = 0.5$ (circles) and $R = 0.7$ (triangles) and for the k_{T}-cluster algorithm using the E_{T} scheme (crosses) for the following thresholds on calorimeter cells: a) $E_T^{\mathrm{tower}} > 0.5$ GeV, b) $E^{\mathrm{tower}} > 1$ GeV, and c) $E^{\mathrm{tower}} > 1.5$ GeV.

11.6.4 Parton-level corrections

In the CDF experiment, it has been shown that total energy of particles in various cones in the vicinity of a parton is well simulated by PYTHIA, enabling the parton energy scale to be corrected to the particle-level jet energy scale via Monte Carlo simulation derived correction factors ($k_{\mathrm{ptcl}} \equiv p_{\mathrm{T}}^{\mathrm{jet}}/p_{\mathrm{T}}^{\mathrm{parton}}$). Figure 11.27 shows these corrections as a function of quark or gluon p_{T}. For quark jets and a cone radius of $R = 0.7$, the correction to parton energy is insignificant. The η dependence of the parton corrections are shown in Figure 11.28.

The parton level corrections are different for light quark and gluon jets. The parton level correction for the mixture of quark and gluons (corresponding to QCD sample, for instance) can be obtained with expression

$$K_{q+g\ \mathrm{mixture}} = \frac{f \times K_q + K_g}{f+1}, \tag{11.2}$$

where f is the ratio of the number of quarks and gluons in the dataset. The parton level correction for the any channel can be derived from the correction for quarks and gluons, supposing the relative ratio of quarks and gluons. The determination of the relative ratio of quarks and gluons in the data is expected to be difficult and would lead to additional systematic errors on the jet energy scale. The b jet has different fragmentation compared with that from both light quarks and gluons and, thus, requires a special set of corrections. The first estimation of the parton level corrections will be obtained from γ+jet and W$\rightarrow$ jet + jet (via $t\bar{t}$) samples. In each of these samples, parton balance can be measured with reasonably high accuracy. In applying the calibration, however, one needs to take into account the differences between quark and gluon jets.

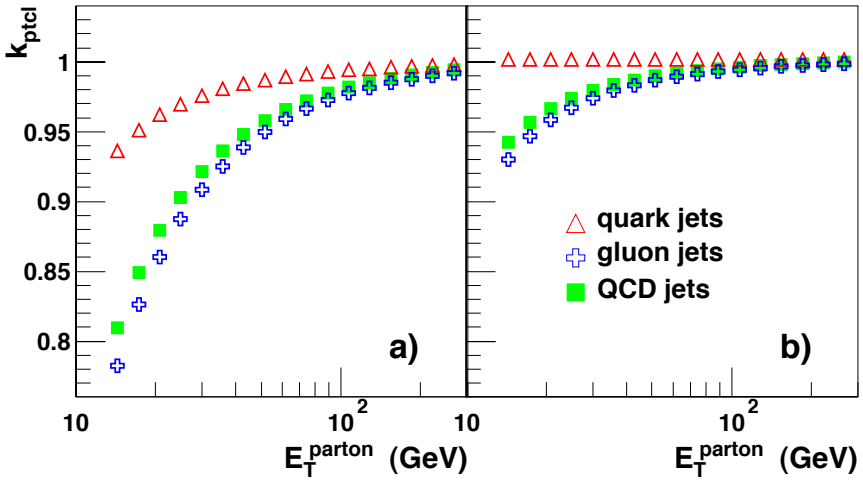

Figure 11.27: Ratio of transverse momenta of particle-level jets to the transverse momenta of the initial partons for QCD, quark and gluon jets collected in cones of (a) $R = 0.5$ and (b) $R = 0.7$ at $|\eta_{\rm jet}| < 1.5$ as a function of transverse parton energy. These corrections are computed with PYTHIA (version 6.214).

11.6.5 Jet energy scale calibration using the W boson mass constraint in top quark events

In the search for new physics, or when aiming for precise measurements, the knowledge of the absolute energy scale of reconstructed jets originating from quarks is crucial. As demonstrated in [264] one can invert the process and determine, via the well-measured W boson mass, the absolute energy scale of reconstructed jets from the decay $W \to q\bar{q}$. An estimate is made of the precision that can be obtained on the absolute jet energy scale using the hadronic decaying W bosons in a selected sample of $t\bar{t} \to bW\bar{b}W \to bq\bar{q}\bar{b}\mu\nu_\mu$ events.

A study of this calibration technique using 3×10^6 inclusive $t\bar{t}$ events has been performed [279]. With a Next-to-Leading Order cross-section of about 800 pb, this reflects 3.75 fb^{-1} of integrated luminosity. It was found that the W+jets background contribution was negligible after the event selection. The inclusive single muon trigger is applied as described in the DAQ TDR [8].

As an example, the jets in the final state are reconstructed with the Iterative Cone algorithm using an opening angle of ΔR = 0.5. Seeds for the cones where selected from all towers above a pseudorapidity dependent energy threshold determined from the average underlying event energy deposits. An initial jet calibration has been applied as taken from a Monte Carlo study.

In order to discriminate between jets originating from the heavy b-quarks compared to the light quarks, a b-tag probability was constructed from the combined b-tag discriminant variable (Section 12.2.3). The lepton is reconstructed and identified using the methods described in [280]. A combined likelihood ratio of several observables is determined for each muon in the final state in order to enhance the purity of choosing the correct lepton from the leptonic W decay. The muon having the largest combined likelihood ratio value is taken as the hard lepton of interest.

A simple pre-selection was applied on the event requiring at least four jets with pseudora-

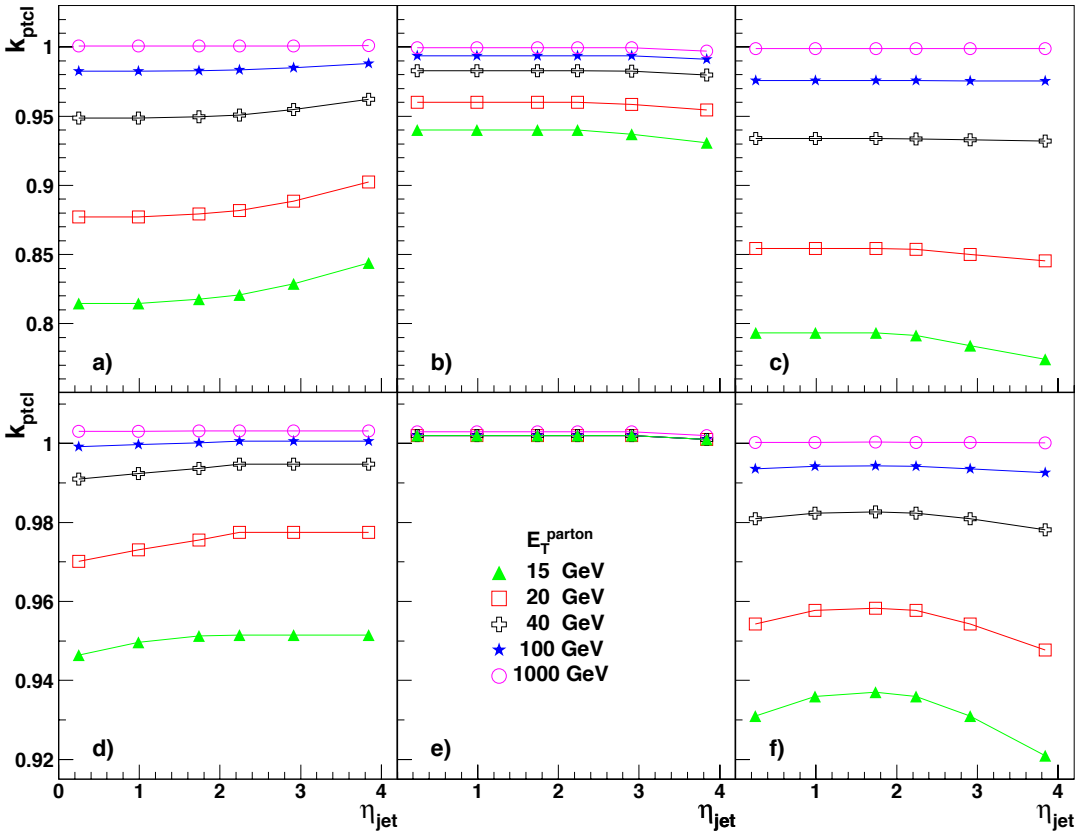

Figure 11.28: Ratio of transverse momenta of particle-level jets to the transverse momenta of the initial partons for QCD, quark and gluon jets collected in cones of (a) $R = 0.5$ and (b) $R = 0.7$ as a function of jet pseudorapidity for the different energies of parton. These corrections are computed with PYTHIA (version 6.214).

pidities in the range of the tracker or $|\eta| < 2.4$ and a raw or not calibrated E_{T} above 10 GeV. The jets must have a flight direction through the tracker to allow for a proper performance of the b-tagging algorithm. At least one muon is required within the tracker acceptance of $|\eta| < 2.4$ and with a combined likelihood ratio value large than 0.01.

The event is required to have exactly 4 jets with a calibrated p_{T} above 30 GeV/c. Exactly two of these four jets need to have a b-tag probability larger than 60%, the remaining two jets should not exceed a probability value of 30% . The latter two are assigned to the W boson decay, resulting in an efficiency of 80% for choosing the correct jet combination. It is also required that the cones of these four jets do not overlap in (η, ϕ) space. The reconstructed hard lepton has to have a transverse momentum p_{T} exceeding 20 GeV/c. The two jets assigned to the W boson are required to have a p_{T} smaller than 120 GeV/c and this two jet system together with one of the two b-tagged jets should have a top quark mass below 350 GeV/c^2. In order to be more robust the angle between these two light quark jets should exceed 1 radian. For 1fb^{-1} and in the W boson mass window between 0 and 160 GeV/c^2 this event selection results in 713 expected signal events and 152 expected $t\bar{t}$ events with different decay channels.

From the light quark jets the W boson mass can be determined. This is shown in Figure 11.29. The invariant W mass spectrum can be fitted with a simple Gaussian function $G(m_W, \sigma)$

and the mean value m_W can be taken as an estimate of the reconstructed W boson mass. It is observed that the estimated W boson mass does not agree with the world average, $M_W = 80.426 \pm 0.034$ GeV/c^2 [119].

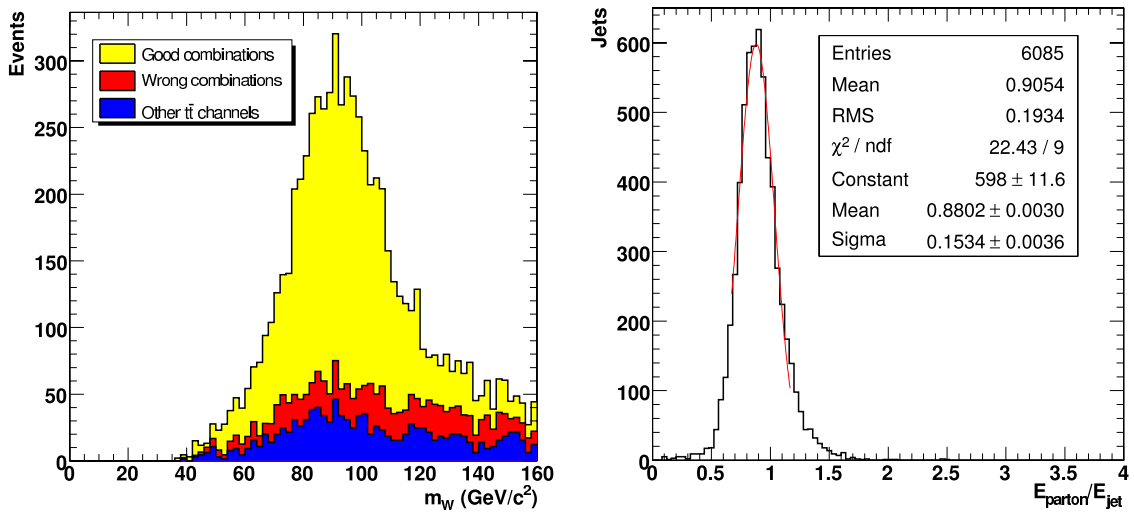

Figure 11.29: Distribution of the W boson mass including combinatorial and process backgrounds, together with the distribution of $E_{\text{parton}}/E_{\text{jet}}$ obtained from simulation truth. The background samples are rescaled to the integrated luminosity of the signal sample.

The W mass spectrum can also be constructed from jets which obtain an extra relative calibration shift ΔC (in %) on their energy scale, $E_{\text{new}} = (1 + \Delta C)E_{\text{jet}}$. The direction of the jet is kept invariant for this rescaling procedure, while the magnitude of its momentum is rescaled in order to keep the E/p ratio of the jet invariant. Therefore one can fit several m_W spectra with different values of ΔC. The value of ΔC which results in a fitted m_W in agreement with the precise world average M_W is the best estimate of the correction needed on the absolute jet energy scale for jets originating from light flavoured partons. Using this method on `MCJet` pre-calibrated jets a value of $\Delta C = -12.9 \pm 0.4\%$ is obtained. The result is obtained by rescaling the event samples to an integrated luminosity equal to the one of the signal sample.

From the selected signal events one can identify the light quark jets with an angular criterion of $\Omega_{jet,parton} < 0.2$ rad where Ω is the angle between the vectors of the jet and the parton in the (θ, ϕ) metric. From these jets the reconstructed and pre-calibrated energy E_{jet} can be compared to the generated parton energy E_{parton}, as shown in Figure 11.29. The average value of $(E_{\text{parton}}/E_{\text{jet}}) - 1$ can be taken as the true energy scale correction to be estimated, denoted as ΔC_{true}. This value is found to be ΔC_{true} = -12.0% . The bias can therefore be defined as $\Delta C_{\text{bias}} = \Delta C - \Delta C_{\text{true}}$ = -0.9 $\pm$ 0.5 % . The resulting bias could be induced by the fact that the jet energy scale correction depends on the kinematics of the $W \to q\bar{q}'$ decays used. Therefore extensions of this inclusive method should be studied, for example by estimating the measured jet energy scale correction as a function of the p_{T} of the jets.

Although the trigger requirements are not the same and there are other reconstruction aspects, it is safe to assume that the available statistics can almost be doubled when including

also the $W \to e\nu_e$ decay. Using this doubling of data, the uncertainty on the estimation of ΔC can be rescaled to an integrated luminosity of 1 fb^{-1} resulting in an expected statistical uncertainty of 0.6%. The jets in the selected sample used to obtain this result have an average transverse energy, E_{T}, equal to 57 GeV and an average energy, E, equal to 79 GeV.

The influence of pile-up is found to be ΔC(PU-noPU) $= -3.1\%$, estimated by using simulated signal event samples with and without low luminosity pile-up collisions. This is the average effect on the energy scale on each reconstructed jet from the inclusion of pile-up collisions in-time with the bunch crossing containing the hard-Q^2 event. With the advent of efficient pile-up subtraction methods, the magnitude of this effect should decrease. The influence of the combinatorial and process background is estimated from a W boson mass spectrum with and without including the background. For both the difference in ΔC is found to be on the level of 0.1% . Systematics arising from the applied b-tagging algorithm will basically change this combinatorial and process background contribution and the effect is therefore partially included in the systematic uncertainties described. The total systematic uncertainty on ΔC is conservatively estimated to be equal to 3.1% and completely dominated by the effect of pile-up.

A similar method using both the W boson mass and the top quark mass constraints can be exploited to estimate the absolute jet energy scale of jets originating from b-quarks. On an event-by-event basis one can force the 2 light quark jets from the W decay to obtain the world average measured W boson mass. The energy scale of the b quark can then be adapted to fit the world average measured top quark mass.

11.7 Association of jets with the signal vertex

One of the most experimentally challenging aspects of LHC physics is the issue of in time pile-up, where minimum-bias interactions can introduce additional jets into the event. A technique to efficiently associate jets with the signal vertex is needed to reduce the large luminosity-dependent instrumental background from pile-up jets. The CMS tracker can provide this information by associating reconstructed charged tracks to primary vertices and to jets. To associate a jet with a signal vertex, defined by a lepton or other high-p_{T} tracks of interest, a significant fraction of the tracks in the jet should originate from this primary vertex.

Two approaches have been investigated to test whether jets originate from the signal vertex or not. They differ in the use of the calorimeter jet energy measurement.

- Method A:
  1) The variable α_{jet} is determined for each jet as the ratio of the sum of transverse momenta of all tracks found inside the jet cone and having the same vertex as the signal (by a z matching residual) to the transverse momentum of the jet as measured by the calorimeters:

$$\alpha_{\mathrm{jet}} = \frac{\sum p_{\mathrm{T}}\ (\text{track in cone})}{E_{\mathrm{T}}\ (\text{jet})}. \tag{11.3}$$

  2) If $\alpha_{\mathrm{jet}} > \alpha_0$, this jet is assigned to the signal vertex.
- Method B:
  1) The variable β_{jet} is determined for each jet as the ratio of the sum of transverse

momenta of all tracks found inside the jet cone and having the same vertex as the signal to the transverse momentum of all tracks inside the jet cone:

$$\beta_{\rm jet} = \frac{\sum p_{\rm T}\ (\text{track associated with jet})}{\sum p_{\rm T}\ (\text{track in cone})} \tag{11.4}$$

2) If $\beta_{\rm jet} > \beta_0$, this jet is assigned to the signal vertex.

11.8 Jet energy correction using charged tracks

It has been shown that precision charged particle tracking may be used to significantly improve and linearize the jet energy resolution [252, 253]. Energy flow techniques have also been successfully used to improve jet measurements at HERA and LEP [281, 282]). Nevertheless, such corrections can be quite complex and are expected to evolve with time as the detector response is better understood.

An initial jet correction procedure has been identified for CMS [283, 284] which corrects for tracks swept out of the jet cone by the 4 T magnetic field and replaces the expected calorimeter response for those charged tracks with the corresponding energy determined from the more accurate tracker momentum measurement. The expected calorimeter response for such charged tracks is based on test beam measurements and Monte Carlo simulations. This "calorimetry-plus-tracker" correction procedure increases the jet energy since the (underestimated) response from the calorimetry to charged hadrons is replaced with the corresponding track momenta, as measured in the tracker, as well as adding the out-of-cone energy (from charged tracks).

Samples of QCD dijet events, simulated in different bins of $\hat{p}_{\rm T}$ were simulated with PYTHIA and digitized without simulating the underlying event and without simulating pile-up [284]. Jets are found at the generation and reconstruction levels using the iterative cone algorithm with $R = 0.5$. A comparison was then made of the reconstructed jet with the Monte Carlo generated jet. The dependence of the jet resolution on the Monte Carlo generated jet energy (for jets generated with $|\eta| < 0.3$) is shown in Figure 11.30 for "calorimetry" jets. For comparison, the dependence of the ratio of reconstructed jet energy to Monte Carlo generated jet versus Monte Carlo generated jet energy (again, for jets generated with $|\eta| < 0.3$) is shown in Figure 11.31 for "calorimetry-plus-tracker" jets. The linearity of the response is seen to improve by including track corrections to the jets. Indeed, approximately half of the resolution improvement is a result of recovering the energy from out-of-cone charged tracks.

To illustrate the expected improvement from using the track corrections, Z' bosons ($m = 120\ \mathrm{GeV}/c^2$) decaying into light quarks were fully simulated and digitized with low-luminosity pile-up. The Z' mass was reconstructed from the 2 leading jets. Figure 11.32 shows the ratio of the reconstructed to the generated Z' mass with, and without, the track corrections. The ratio is 0.88 ± 0.12. Including charged-track corrections, the ratio improves to 1.01 ± 0.12, correcting the mass scale, and improving the resolution by about 10%.

11.9 Jet reconstruction in heavy-ion collisions

Jets from heavy-ion collisions at the LHC may provide information about parton propagation through a quark-gluon plasma. The main challenge with jet reconstruction in heavy-ion

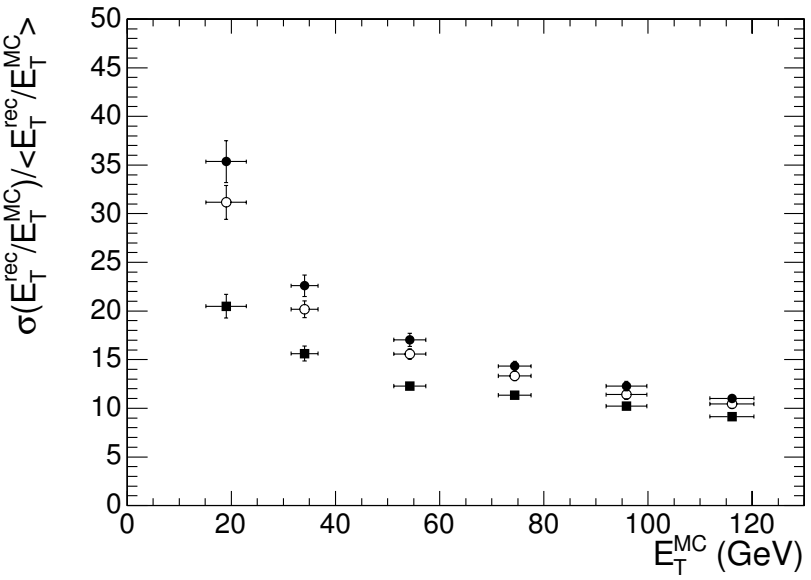

Figure 11.30: The jet E_{T} resolution as a function of generated jet E_{T} for reconstruction with calorimeter only (full circles), addition of out-of-cone tracks (open circles), and further charged track response corrections (full squares).

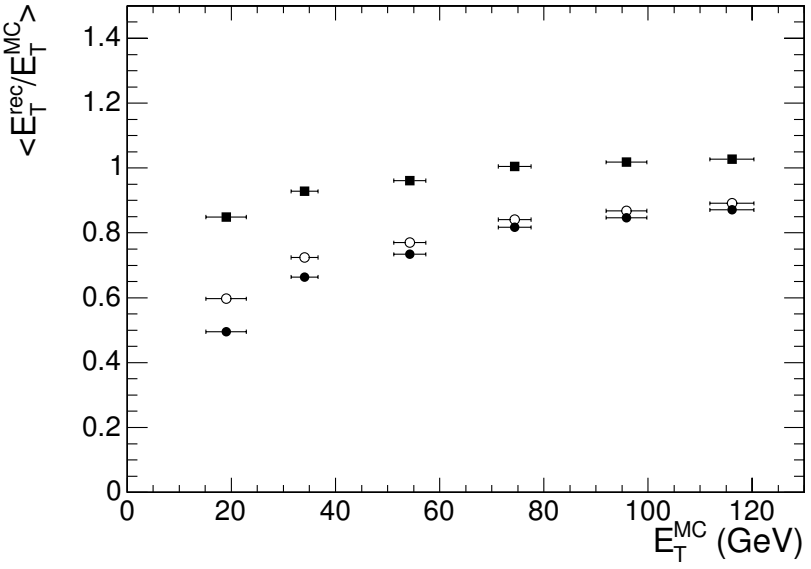

Figure 11.31: Ratio of reconstructed to generated jet E_{T} as a function of the generated jet E_{T} for reconstruction with calorimeter only (full circles), addition of out-of-cone tracks (open circles), and further charged track response corrections (full squares).

collisions is the subtraction of background arising from fluctuations of the transverse energy flow due to the large multiplicity of secondary particles in the event [285]. Predictions vary from 1400 to 8000 charged particles per unit of rapidity in central Pb-Pb collisions at the LHC.

The original jet finding algorithm was developed for reconstructing hard jets (E_{T} of order 100 GeV) in heavy-ion collisions, where particles produced in a typical collision deposit transverse energy up to 10 GeV in every calorimeter tower. The algorithm allows subtraction of

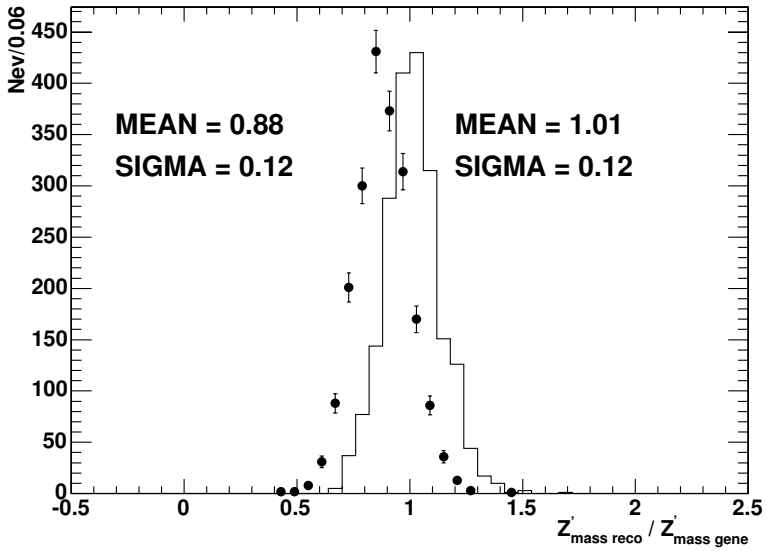

Figure 11.32: Ratio of the reconstructed to the generated Z' mass with calorimetry only (solid circles) and with track corrections (histogram).

the background energy due to the underlying event energy flow and identification of the hard jets on an event by event basis. In this study, jet finding is done with the background subtraction algorithm currently implemented in the CMS reconstruction software (ORCA).

11.9.1 Background subtraction algorithm

In heavy-ion collisions at the LHC, fully formed jets are expected to be visible for the first time in nuclear collisions with transverse energies well over 100 GeV. A jet finding algorithm has been developed to search for clusters above the average transverse energy flow.

- The average transverse energy of tower i ($\langle E_{\mathrm{T}}^{i} \rangle$) and its dispersion ($\sigma_i$) are calculated.
- All tower transverse energies are recalculated by subtracting the average tower energy plus a factor k times its dispersion ($E_{\mathrm{T}}^{i} - \langle E_{\mathrm{T}}^{i} \rangle - k\sigma_i$). If the value of the transverse tower energy after subtraction becomes negative, it is set to zero.
- Using the corrected tower energies, jets are found with the iterative cone algorithm.
- The average tower energies and dispersions are recalculated again using only towers outside of the jets. The original tower energies are used in this calculation.
- All tower energies are recalculated by subtracting the revised average tower energy plus k times its dispersion. If the value of the transverse tower energy after subtraction becomes negative, it is set to zero.
- Using the revised tower energies, jets are found with the iterative cone algorithm one more time.

A factor $k = 1$ is used in this study to compensate the positive bias in the reconstructed jet energy due to suppression of towers with the negative energy. This scheme gives an

approximation for the reconstructed jet energy in Pb-Pb close to the energy obtained in pp.

11.9.2 Performance of jet reconstruction

Dijet events from pp collisions generated with PYTHIA are superimposed on 5.5 TeV Pb-Pb events which are generated with the HIJING Monte-Carlo generator using the default setting (quenching on) with $dN_{\rm ch}/dy|_{y=0} = 5000$. The combined events were fully digitized.

Jet reconstruction is studied using the background subtraction algorithm described above. The threshold for the reconstructed jet energy is set at 30 GeV. Only the highest $E_{\rm T}$ jet in an event is used for further analysis. The correlation between the reconstructed and generated jet $E_{\rm T}$ for Pb-Pb and pp events is shown in Figure 11.33. On average, the measured jet energy in Pb-Pb collisions is the same as that in pp. In other words, the background subtraction algorithm gives a reconstructed jet energy which is the same for pp (without background) and for Pb-Pb (with background) interactions.

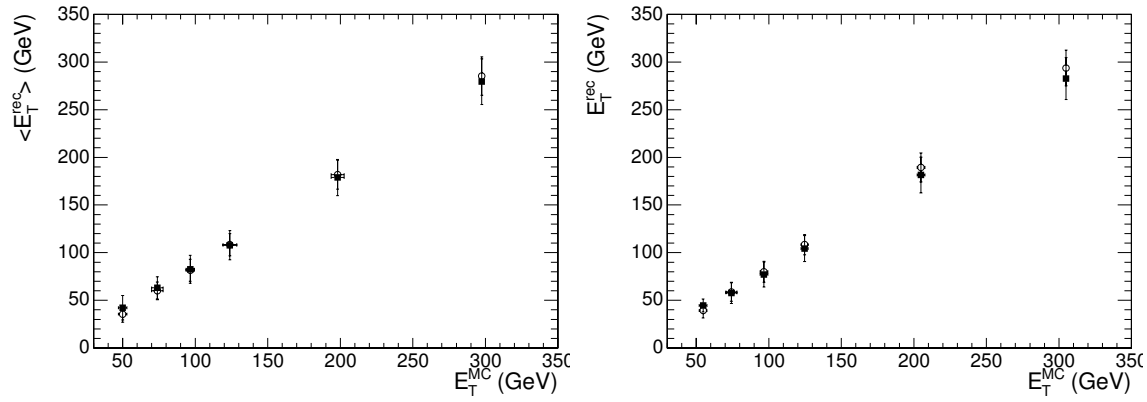

Figure 11.33: The correlation between the average reconstructed and the generated jet transverse energies in Pb-Pb (full squares) and pp (open circles) events in the barrel (left) and endcap (right). The error bars are the dispersion of jet energy distribution.

The jet energy resolution is defined as $\sigma(E_{\rm T}^{\rm reco}/E_{\rm T}^{\rm MC})/\langle E_{\rm T}^{\rm reco}/E_{\rm T}^{\rm MC}\rangle$, where $E_{\rm T}^{\rm reco}$ and $E_{\rm T}^{\rm MC}$ are the reconstructed and generated jet transverse energies. Figure 11.34 shows the jet resolution as a function of $E_{\rm T}^{\rm MC}$. The jet energy resolution is degraded by approximately 20% in high multiplicity central Pb-Pb collisions compared to pp.

Since the azimuthal angle and the rapidity distributions of jets is of particular interest for jet quenching observables in heavy-ion collisions, spatial resolution is important. For 100 GeV jets, the η and ϕ resolutions are 0.028 and 0.032 correspondingly.

The subtraction procedure allows the identification and measurement of jets in heavy-ion collisions using only CMS calorimeters with very high efficiency and purity. Jets reconstructed in central Pb-Pb collisions with $E_{\rm T} > 30$ GeV, that are within $\Delta R < 0.25$ around the direction of the generated MC jet are considered as true QCD jets. The efficiency of jet reconstruction in central Pb-Pb collisions is estimated as the fraction of events with such true QCD jets among all the generated events. The efficiency of finding a true QCD jet is nearly 100% for $E_{\rm T} = 75(100)$ GeV jets in the barrel (endcap) region.

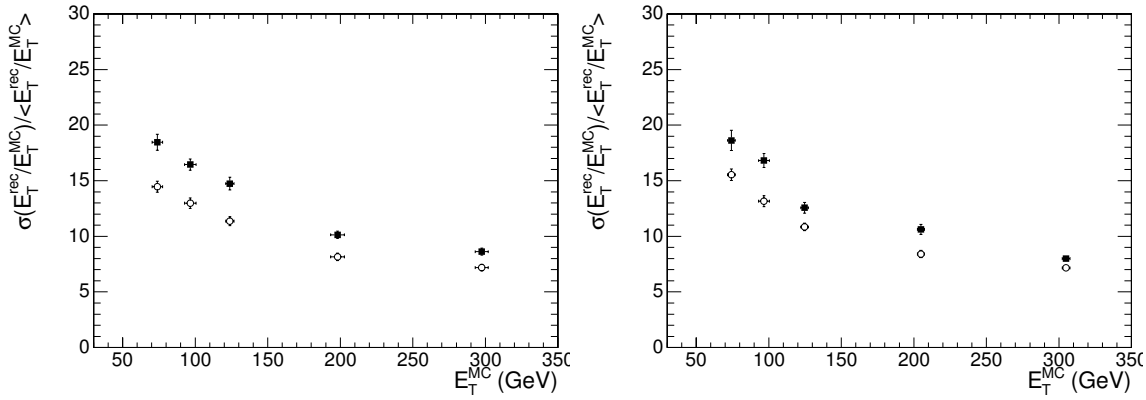

Figure 11.34: Jet energy resolution in Pb-Pb (full squares) and pp (open circles) events in the barrel (left) and endcap (right) regions.

The purity of the reconstructed jet sample is defined as the number of events with true QCD jets divided by the number of events with at least 1 reconstructed jet (fake or real) with transverse energy above 30 GeV. Beyond E_{T} = 50 GeV (75 GeV) jets, the purity is nearly 100% for the barrel (endcap).